MELTING LAYER ANALYSIS OF IN-SITU OBSERVATIONS OBTAINED FROM MULTIPLE FIELD PROJECTS

by

Logan Twohey
Bachelor of Science, University of Louisville, 2019

A Thesis

Submitted to the Graduate Faculty

of the

University of North Dakota

in partial fulfilment of the requirements

for the degree of
Master of Science

Grand Forks, North Dakota

July
2022

LIST OF FIGURES

LIST OF TABLES

ACKNOWLEDGMENTS

Acknowledgements.

Data and software availability in repository. NASA data are available at NASA DAC archive.

ABSTRACT

The process of melting snow as clouds precipitate is important for storm evolution. The atmospheric layer where melting occurs has largely been studied with radar observations that investigate the bright band region; however, in-situ observations are necessary to improve and verify these radar observations. In-situ observations during recent NASA field campaign are reviewed to obtain aircraft profiles of the melting layer. A total of thirty-three melting layer cases are analyzed for changes in area ratio and particle size distribution from above, within, and below the melting layer. Additionally, the effect relative humidity in the melting layer is analyzed. The area ratio begins to increase when the ice-bulb temperature is above 0 °C, which indicates the area ratio can depict the melting layer top. Only two of the thirty-three cases analyzed have a 0 °C quasi-isothermal layer nearby the melting layer, which indicates diabatic cooling from melting does not frequently produce such a layer as has been commonly reported. Additionally, there is a lack of enhanced aggregation within the melting layer, which has been hypothesized as a potential cause of the radar bright band signal. Large hydrometeors concentration decreases from above to below the melting layer; however, the small hydrometeors concentration does not commonly increase, which suggests that hydrometeors evaporate and the concentration is shifted to hydrometeors smaller than 500 µm. Exponential spectrum fits to the particle size distribution are largely variable; however, the slope parameter commonly increases in the melting layer, which suggests there is no enhanced aggregation. Still, there is occasionally a small increase in the maximum hydrometeor diameter within the melting layer. Additional analysis could compare radar reflectivity changes to the melting layer observed particle spectrum changes.

CHAPTER 1

INTRODUCTION

1.1 The Melting Layer

The melting layer in cold precipitating cloud systems is the layer where frozen hydrometeors transition from ice to liquid as they fall. The melting layer top has typically been taken to be 0 °C since above this temperature snow starts to melt. However, aircraft measurements (Heymsfield et al. 2002, 2015) have indicated that snow only starts melting at 2 °C in low relative humidity environments. Hence, the wet-bulb temperature of 0 °C is a better representation of the top of the melting layer (Ding et al. 2014; Iversen et al. 2021). However, Heymsfield et al. (2021) determined that melting only begins when air has an ice-bulb temperature warmer than 0 °C because when air has a temperature that is warmer than 0 °C, and an ice-bulb temperature colder than 0 °C, hydrometeors sublimate. A schematic of the relationship between air temperature, relative humidity, the sublimation zone, and melting zone for two different pressure levels is shown in figure 1 of Heymsfield et al. (2021). At a pressure of 1,000 hPa and relative humidity of 70 percent, snow only starts melting when the air temperature is a little warmer than 2 °C. The effect of relative humidity on melting is more pronounced at lower pressures. For example, at 500 hPa and 90 percent relative humidity, snow starts melting at an air temperature of approximately 1.5 °C, while at 1,000 hPa melting starts at 1.0 °C. Hence, it important to not simply use 0 °C to determine the top of the melting layer. Recent studies indicate using the 0 °C ice-bulb isotherm as melting layer top is the best representation because it accounts for air temperature, relative humidity, pressure, and the phase of the hydrometeor.

In subsaturated air, snow falls farther before melting, which increases the depth of the melting layer compared to saturated air. McFarquhar et al. (2007) found that melting occurred within 300 m when near or at saturation, while the melting layer was 500 m for subsaturated air. The melting layer depth is an important feature that can affect the thermal structure and dynamics of clouds. Findeisen (1940) discovered diabatic cooling associated with melting creates a 0 °C isothermal layer. Wexler et al. (1954) showed that diabatic cooling is significant in lowering the freezing level, which deepens the melting layer and extends the survival of snow below the freezing level. Additionally, the unstable lapse rate created by diabatic cooling causes subsidence of the cold air. For example, the cooling, and the associated subsidence, can cause surface temperature to drop up to 4.4 °C (8 °F).

The 0 °C isothermal layer produces mesoscale circulations. Atlas et al. (1969) investigated these mesoscale circulations and the relation to precipitation intensity. Horizontal inhomogeneity of diabatic cooling due to melting snow creates horizontal pressure perturbations in the melting layer, which caused mesoscale oscillations of the wind (Atlas et al. 1969). These mesoscale wind perturbations have a maximum on the low pressure side of storms and the magnitude increases with precipitation intensity. Small scale wind perturbations also caused wave motion. Stewart et al. (1984) took atmospheric soundings of a melting layer that produced a 200 m thick isothermal layer. In the isothermal layer, equivalent potential temperature increased with height, whereas below the isothermal layer, it decreased with height. The diabatic cooling and associated conditionally unstable layer created a dynamic response that could induce turbulence or shallow embedded convection. Lin and Stewart (1986) confirmed previous findings of non-uniform, diabatic cooling producing mesoscale circulations. The circulations were similar to sea breeze circulations; however, were forced by a horizontal temperature perturbation aloft, where the updrafts in the isothermal layer created outflow below and inflow above. The magnitude of the circulation was found to be related to the amount of cooling. Willis and Heymsfield (1989) hypothesized a separation of dynamics above and below the melting layer, with a transition region in the melting layer. In agreement with previous observations, ascent would occur above the melting layer and descent below. From Lin and Stewart (1991), updrafts arising from circulations caused by melting may enhance precipitation in saturated environments.

The amount of diabatic cooling associated with the melting layer has been shown to affect frontogenesis. Carbone (1982) suggested the diabatic forcing associated with cooling sustained frontogenesis by establishing a resonance with cold air advection and frontal forcing. Szeto and Stewart (1997) investigated frontogenesis with a 2D cloud model that contained detailed cloud microphysics to resolve cloud-scale and mesoscale processes. A positive feedback between thermal and dynamic processes was developed. Perturbations enhanced baroclinicity and accelerated frontogenesis when diabatic forcing from latent cooling created a coincidentally located downdraft causing enhanced convergence. Accelerated frontogenesis resulted in stronger updrafts and more snow, causing stronger diabatic forcing due to increased melting snow. The feedback was broken when the enhanced snowfall intensity became decoupled from the frontal forcing. It should be pointed out that Szeto and Stewart (1997) identified limitations of the study that included a lack of precipitation-associated diabatic forcing and consequences of a 2D model which may exaggerate frontogenesis. Joos and Wernli (2012) budgeted potential vorticity contributors in warm conveyor belts, which is located just ahead of the surface cold front. Consistent with previous studies, they found air parcels gain potential vorticity above the diabatic cooling region. Igel and van den Heever (2014) investigated latent heating effects on warm frontogenesis. While melting was the largest source of latent cooling and led to a separation of dynamics, it was also largely balanced out by latent heating from condensation and cloud droplet nucleation. These patterns were consistent for warm season warm fronts, but different relationships may arise in other situations.

Kain et al. (2000) showed implications of melting layer processes on forecasting precipitation type at the surface. They studied a case where melting-induced cooling led to an unexpected transition from rain to heavy snow, which resulted in a poorly forecasted event that had a significant societal impact. Surface observations showed that temperatures only fell in areas of persistent precipitation and never decreased below 0 °C. Snow melting led to the rapid temperature decrease at the surface and the transition from rain to snow. An improved understanding of the microphysical processes in the melting layer of precipitating clouds can lead to improved forecasting of such events.

1.2 Radar Observations of the Melting Layer

Many previous studies have analyzed the melting layer using radar observations. Radars observe a bright band signal caused by an increase of radar reflectivity by up to about 10 dBZ due to hydrometeor melting. Stewart et al. (1984) found the location of the bright band maximum to be at 2 °C, which varied from 250 m to 300 m below the top of the melting layer. Rainfall rate determines the relative magnitude of the bright band (Fabry and Zawadzki 1995; Kain et al. 2000) and its vertical width (Klaassen 1988). The width of the bright band increases with higher rain intensity due to a deeper isothermal layer (Klaassen 1988).

Austin and Bemis (1950) first proposed that the cause of the bright band was due to coalescence (aggregation) and melting of snowflakes. However, Battan (1973) concluded the increase in radar reflectivity is due to a sharp increase in the dielectric constant when hydrometeors begin to melt. Below the bright band peak, partially melted snowflakes shrink causing a decrease in reflectivity, which eventually matches that of the rain falling below the melting layer. Willis and

Heymsfield (1989) concluded that large aggregates that initially survive in the melting layer before fully melting were responsible for the bright band. More recent studies have since suggested the increase in dielectric constant cannot sufficiently explain the magnitude of the bright band (e.g., Klaassen 1988; Fabry and Zawadzki 1995; Heymsfield et al. 2015). Fabry and Zawadzki (1995) found the dielectric constant change leaves 10 dB of the bright band magnitude unaccounted. Some of the reflectivity increase is likely due to shape effects due to nonsphericity of melting hydrometeors at stratiform rain rates may increase reflectivity. Additionally, the coupling of aggregation and breakup, along with precipitation growth, may contribute a relatively small contributors to the bright band. The relative extent to which each of these physical processes contributes to the magnitude of the bright band remains an unsolved issue.

Baeck and Smith (1998) found the bright band caused one radar's rainfall estimates to be nearly three times higher than another radar's estimates that did not intercept the bright band. The importance of correcting for this rainfall overestimation due to the bright band has been highlighted; however, rainfall estimates were sometimes overcorrected (Harrison et al. 2000). Quantifying the different contributions to the bright band is necessary to improve rainfall estimates.

1. 3 Laboratory Experiments and Numerical Models

Laboratory experiments provide additional information for understanding the melting layer. Individual snow hydrometeor observations show an initial stage of uniform melting, followed by a stage where the melting rate depends on meltwater thickness covering the ice (Knight 1979). Matsuo and Sasyo (1981) released collected snowflakes in a vertical wind tunnel. Contrary to results of Knight (1979), meltwater did not fully cover the snowflake's surface. Instead, a ragged ice surface was maintained during melting and the ice structure of a snowflakes did not easily collapse during melting. To reduce the chance of snowflakes breaking, Fujiyoshi (1986) collected snowflakes on a silicone oil layer. Their melting snow observations indicated melting first occurred on the bottom side of a snow crystal. The top side melted at a slower rate due to less efficient heat transfer, as well as latent heat causing the air temperature on the top side to be cooler. Water droplets appeared at the tips of melting forks and branches, which were then shed off. In the second stage, the snow crystal top became jagged, while the edges rapidly melted and formed droplets that would be shed off. Similar to Matsuo and Sasyo (1981), the surface became jagged and holes formed on the melting crystal during the third stage. In the fourth stage, the melting crystal becomes irregularly shaped but was smooth and contained no holes. In the final stage, crystal became round and presumably fully melted. Similarly, Mitra et al. (1990) used wind tunnel experiments to depicted four distinct stages of melting: 1) intense melting on the edges and bottom, with small drops formed at the crystal branch tips; 2) surface tension effects and capillary forces directed meltwater to the linkages of crystal branches, and the melting crystal became ragged while the meltwater both held the crystal together and compacted the shape; 3) the structure was rearranged to have small branches on the crystal's interior and meltwater flows to the main crystal branches; 4) the crystal became drop shaped as the ice frame collapsed and meltwater covered the melting snowflake completely.

Results from laboratory experiments have been used in microphysics parameterization schemes (e.g., Iversen et al. 2021). Matsuo and Sasyo (1981) developed a model to depict the microphysics of melting snow where the rate of crystal radius decrease was calculated using the air temperature, hydrometeor shape and fall speed. Additionally, ice density was found to be an important factor Klaassen (1988). Szyrmer and Zawadzki (1999) developed a numerical model and bulk microphysical parameterization scheme that agreed with observations; however, there was uncertainty in the morphology of melting snowflakes, which included snow parameters (shape, density, fall speed, etc.). Leinonen and von Lerber (2018) developed a 3-D numerical model of a single crystal melting. Riming was found to have a significant impact on melting. Rimed hydrometeors were more porous during melting, absorbing more meltwater and becoming less prone to breakup. Utilizing a one-dimensional model of melting snow, Carlin and Ryzhkov (2019) found that relative humidity and environmental lapse rate are important factors in the melting layer and corresponding bright band thickness.

1.4 In-situ Observations

There have been relatively few in-situ melting layer observations Heymsfield et al. (2015). Utilizing optical array probe measurements, Stewart et al. (1984) found that well-developed bright bands had large aggregates with rounded edges as the most common hydrometeor at 0 °C. At 1.3 °C, hydrometeors were mostly circular; however, non-circular hydrometeors were observed up to 2.0 °C. Small hydrometeors became circular at colder temperature indicating that complete melting proceeds from smaller to larger hydrometeors. There was a slow increase in hydrometeor diameter from -2.5 °C to -1.0 °C, with a rapid increase in size within the 0 °C isothermal layer, which continued until approximately 2 °C where all hydrometeors were round. Stewart et al. (1984) concluded aggregation was the primary cause of decrease in hydrometeor concentration and increase in diameter above and within the melting layer.

Optical array probe measurements are typically fitted to an exponential size distribution

$$N(D) = N_0 e^{-\lambda D} \tag{1}$$

where $N(D)$ is the concentration of hydrometeors, N_0 is the intercept, λ is the slope, and D is the diameter. Measurements near the melting layer were found to be in good agreement with an exponential distribution Stewart et al. (1984). Above the melting layer, the slope parameter decreased with increasing temperature until a minimum of approximately 1 mm^{-1} was reached near 0 °C. Melting prevented the slope parameter from further decreasing and instead the slope parameter increased to approximately 3 mm^{-1} and the intercept parameter decreased within the melting layer until approximately 2.5 °C. Below the melting layer, the intercept parameter increased towards the Marshall-Palmer (Marshall and Palmer 1948) size distribution intercept value of 8×10^{6} m^{-4}.

Willis and Heymsfield (1989) examined the melting layer using aircraft observations taken during spiral descents within a mesoscale convective system. Maximum hydrometeor diameter increased just above and through the isothermal layer due to significant aggregation, while the concentration of smallest hydrometeors decreased. Below the isothermal layer, the concentration of large hydrometeor decreased with melting, although the maximum hydrometeor diameter increased. Relatively few large aggregates survived at temperatures of 5.5 °C and warmer.

McFarquhar et al. (2007) investigated the variability of hydrometeors above, within, and below the melting layer taken during spiral descents through stratiform precipitation. Above the melting layer, the concentration of small hydrometeors decreased while the concentration of large hydrometeors increased, consistent with aggregation. However, the maximum hydrometeor size of approximately 7.0 mm did not vary much with temperature for concentrations greater than 10^{3} m^{-4}. Hydrometeor size distributions were not largely impacted by melting until the melting was almost complete. In a 240 m thick layer starting at 2 °C, hydrometeors with a 4 mm diameter decreased in concentration from 2.2×10^{-7} cm^{-4} to 1.8×10^{-8} cm^{-4}. Relative humidity with respect to ice varied between 92 percent and 105 percent and caused sublimation. Hydrometeors with a size between 128 μm and 512 μm experienced a decrease in concentration that was correlated with relative humidity. McFarquhar et al. (2007) concluded that sublimation caused a decrease in hydrometeor concentrations and maximum diameter of aggregates.

Heymsfield et al. (2015) studied a combination of Lagrangian spiral descents and ascents, and Eulerian descents through the melting layer. Lagrangian flight paths followed a distribution of hydrometeors with altitude if conditions were quasi-steady, whereas Eulerian flight paths were over a fixed geographic point. In high relative humidity environments, there was no significant change in total hydrometeor concentrations above, through, and below the melting layer. Heymsfield et al. (2015) suggested there is little significance in the breakup of melting hydrometeors in and below the melting layer, which would have been expected to enhance hydrometeor concentrations. The lack of concentration enhancement may be a result of aggregation, which Stewart et al. (1984) hypothesized as a cause for decreased concentrations in and just above the melting layer. Consistent with results from Stewart et al. (1984), both the slope and intercept parameters decreased with increasing temperature above the melting layer and through the "critical temperature range" from 0 °C to 1 ℃. As temperatures increased in the melting layer, the slope parameter continued to decrease, which is in contrast to the results from Stewart et al. (1984) where slope parameter was maximized at approximately 0 °C. Aggregation resulted in an increase of maximum diameter through the melting layer. Low relative humidity environments studied by Heymsfield et al. (2015) gave insight on the roles of sublimation vs melting in temperatures exceeding 0 °C. Total hydrometeor concentrations decreased in subsaturated environments suggesting sublimation was occurring. Contrasting clouds at or near saturation, the intercept parameter continued to decrease with increasing temperatures throughout the entire ascent or descent. Sublimation also caused the maximum diameter to decrease below 0 °C.

Heymsfield et al. (2015) used the available high quality hydrometeor images to examine the area ratio within the melting layer. Area ratio is the ratio of the imaged hydrometeor area to the area of a circle fit to the hydrometeor's "fast circle" diameter (more information on the processing is given in Chapter 2). As hydrometeors melt, they become more round and area ratio increases. In a high (91 percent) relative humidity case, melting began around 0.5 °C and the area ratio started increasing for smaller (approximately 400 μm diameter) hydrometeors. In contrast, for the low (70 percent) relative humidity case, the area ratio did not start increasing until approximately 2 °C. In both cases, melting began around an ice-bulb temperature of 0 °C, which is consistent with the proposal to use ice-bulb temperature as an indicator of melting by Heymsfield et al. (2021). Also, both cases had maximum diameter peak just above and near the top of the melting layer, which suggests enhanced aggregation.

Heymsfield et al. (2021) investigated the influence of relative humidity on the melting layer, building on results from Heymsfield et al. (2015). The relative humidity at the air temperature was compared to the relative humidity at the ice-bulb temperature. Noticeable melting commenced when both the ice-bulb temperature fell below the air temperature and when the relative humidity approached the relative humidity at the ice-bulb temperature. Heymsfield et al. (2021) concluded that relative humidity at the ice-bulb temperature was a good indicator of melting. From thirteen flights through the melting layer, precipitation phase and extent of melting was qualitatively assessed. Hydrometeors categorized as "snow" are largely in the sublimation zone, although some "snow mostly" and rarely "mixed" hydrometeors also reside in in the sublimation zone. This is possibly because the ice-bulb temperature was calculated assuming a pressure of 500 hPa. A flight through the melting layer at an air pressure other than 500 hPa alters the actual ice-bulb temperature and thus relative humidity at the ice bulb temperature. Lower pressure enhances the effect of relative humidity on ice-bulb temperature, while at higher pressures the hydrometeors would melt instead of sublimate at a lower temperature given the same relative humidity.

1.5 Objectives

While the snow melting process has been well studied, the process of snow transitioning to liquid drops in precipitating clouds is still not well understood. Due to difficulties associated with the collection of precipitating cloud in-situ observations, research of the melting layer has largely been conducted through remote sensing or numerical simulation. Radar observations of the melting layer typically investigate the bright band radar signal. However, radar observations rely on retrieval algorithms to estimate rainfall rate and hydrometeor size distribution (e.g. Chen and Chandrasekar 2014). In-situ observations provide details to improve retrieval algorithms and verify radar observations. Similarly, the development of microphysics parameterization schemes in numerical models is based on observations (e.g., (Khain et al. 2000; Thompson et al. 2008; Morrison et al. 2015; Iversen et al. 2021). A better model representation of the microphysics based on in-situ observations can help limit assumptions and verify accuracy of simulation results (e.g., Tapiador et al. 2019). Thus, in-situ observations through the melting layer are valuable to improving the representation of microphysical processes within the melting layer.

The objective of this study is to extend previous in-situ analysis of the melting layer by characterizing the hydrometeor size distributions and area ratios using observations from several field campaigns conducted by National Aeronautics and Space Administration (NASA). The field campaigns offer direct observations of precipitating clouds and the melting layer in a variety of environments and storm types. Instruments aboard aircraft profiling the melting layers provide detailed microphysics and thermodynamics data. Data analysis is conducted to determine when hydrometeors have melted and the impact of ambient relative humidity on the melting process, following the methods described by Heymsfield et al. (2015, 2021). The determined relative humidity effect can be incorporated into numerical models to improve weather forecasts. Understanding the evolution of the hydrometeor size distribution through the melting layer can improve rainfall estimates from radar observations, which are critical in the melting layer where there is enhanced radar reflectivity due to the bright band signal.

CHAPTER 2

DATA

2.1 Data Set

The analysis focuses on data from several NASA field campaigns spanning ten years from 2011 to 2020 (Table 1). The University of North Dakota Citation II Research Aircraft was used during four of the five campaigns, and was equipped with a variety of instrumentation for measuring clouds (Figure 1). The NASA P3 Research Aircraft used during IMPACTS is similarly equipped. Instruments aboard aircraft measure standard atmospheric variables (e.g., pressure, altitude, temperature, dew point temperature, relative humidity, etc.), liquid and ice water content, and cloud microphysics parameters. The air temperature is measured by the Rosemount probe and the dew point temperature is measured by the Edgetech (EG&G) Probe.

Table 1: Table summarizing fields projects where cloud sampling was conducted using cloud physics probes. Field project acronyms used are Mid-latitude Continental Convective Clouds Experiment (MC3E); Global Precipitation Measurement (GPM) Cold-season Precipitation Experiment (GCPEX); Integrated Precipitation and Hydrology Experiment (IPHEX); Olympic Mountain Experiment (OLYMPEX); Investigation of Microphysics and Precipitation for Atlantic Coast-Threatening Snowstorms (IMPACTS). The P3_N426NA is the NASA P-3 Orion Research Aircraft and the CitationII_N555DS is the University of North Dakota Citation II Research Aircraft. Small imaging probes ("cloud") detect small hydrometeors with a relatively high resolution and large imaging probes ("precipitation") have a larger sample volume but lower resolution. Probes include the Two-Dimensional Optical Array Cloud (2D-C) Probe; Two-Dimensional Stereo (2D-S) Probe; High Volume Precipitation Spectrometer Version 3 (HVPS3). The (2) HVPS3 indicates two HVPS3 probes were mounted on the aircraft for horizontal and vertical positioning.

Field Campaign	**Dates** (mm/yy)	**Aircraft**	**Cloud**	**Precipitation**
MC3E	04/11 - 06/11	CitationII_N555DS	2D-C	HVPS3
GCPEX	01/12 - 02/12	CitationII_N555DS	2D-C	HVPS3
IPHEX	05/14 - 06/14	CitationII_N555DS	2D-S	HVPS3
OLYMPEX	11/15 - 12/15	CitationII_N555DS	2D-S	(2) HVPS3
IMPACTS	01/20 - 02/20	P3_N426NA	2D-S	(2) HVPS3

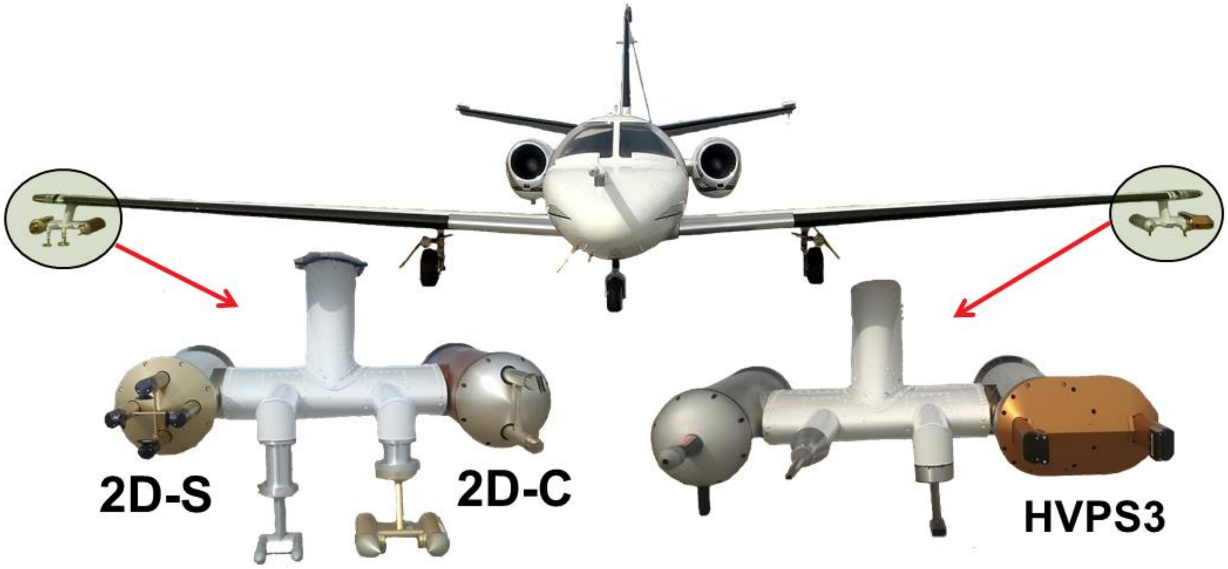

Figure 1: Schematic showing images of the Two-Dimensional Optical Array Cloud (2D-C) Probe, Two-Dimensional Stereo (2D-S) Probe, and High Volume Precipitation Spectrometer Version 3 (HVPS3) mounted on the University of North Dakota Citation II Research Aircraft. Additional probes are shown and mounted on the aircraft but are not highlighted.

The Two-Dimensional Stereo (2D-S) probe (Figure 1) is an optical array probe that images hydrometeors through linear array shadowing (Lawson et al. 2006). The 2D-S probe uses laser beams from two linear 128-photodiode arrays that have an equivalent 10 µm resolution. The two laser beams form a right angle giving horizontal and vertical orientations of the photodiode array. The HVPS3 (Figure 1) is a hydrometeor imaging probe with a single 128-photodioode array of 150 µm resolution (Lawson et al. 1998; Kumjian et al. 2016). Typically, two HVPS3 probes are mounted on aircraft for both horizontal and vertical orientations to match a single 2D-S probe (noted in Table 1). Before the 2D-S probe became available starting with IPHEX, the Two-Dimensional Optical Array Cloud (2D-C) probe (Figure 1) was used for MC3E and GCPEX (Table 1). The 2D-C probe has lower resolution with 32 optical elements, each with a 30 µm resolution (Knollenberg 1981). The 2D-C is only used here for inspecting images to determine the bottom of the melting layer.

2.2 Data Processing

The data from instrumentation aboard aircraft are collected using data acquisition systems such as the Science Engineering Associates (SEA Inc.) model M-300 data acquisition system. The optical array probes such as the Two-Dimensional Stereo (2D-S) probe and the High Volume Precipitation Spectrometer Version 3 (HVPS3) probe use their own individual data acquisition systems. All data acquisition systems have their time synchronized at start of an aircraft flight; although, if there is a syncing issue, it can be resolved in post-processing since GPS based time is always recorded.

The in-situ data are processed with the Airborne Data Processing and Analysis (ADPAA) software package (Delene 2011). ADPAA is an open-source software package that contains several programs for processing and analysis of in-situ data. ADPAA also offers tools such as the Cplot and Aplot programs to quickly visualize American Standard Code for Information Interchange (ASCII) data for analysis. ADPAA utilizes the National Center for Atmospheric Research (NCAR) System for Optical Array Probe (OAP) Data Analysis version 2 (SODA2) for processing OAP data including the 2D-S and HVPS3. Automated processing in ADPAA creates 1 Hz temporal frequency ASCII data files from the raw data for area ratio, aspect ratio, concentration, counts, and cross-sectional area. The processing done by SODA2 implements several corrections for hydrometeor sizing and measurements. Out of focus images and artifacts are removed during processing. Hydrometeors are sorted into bins of varying size for the 2D-S and HVPS3 (Table 2). The 2D-S is limited to hydrometeors up to 2,000 µm in diameter and the HVPS3 is limited to hydrometeors up to 30,000 µm in diameter (Table 2).

Table 2: Table showing the size range of the bins from the System for Optical Array Probe (OAP) Data Analysis (SODA2) processing of the Two-Dimensional Stereo (2D-S) probe images and the High Volume Precipitation Spectrometer Version 3 (HVPS3) probe images.

	2D-S	**HVPS3**

Bin *[#]*	**Size Range** *[μm]*	**Midpoint** *[μm]*	**Bin Size** *[μm]*	**Size Range** *[μm]*	**Midpoint** *[μm]*	**Bin Size** *[μm]*
1	5-15	10	10	200-400	300	200
2	15-25	20	10	400-600	500	200
3	25-35	30	10	600-800	700	200
4	35-45	40	10	800-1000	900	200
5	45-55	50	10	1000-1200	1100	200
6	55-65	60	10	1200-1400	1300	200
7	65-75	70	10	1400-1600	1500	200
8	75-85	80	10	1600-1800	1700	200
9	85-95	90	10	1800-2200	2000	400
10	95-105	100	10	2200-2600	2400	400
11	105-125	115	20	2600-3000	2800	400
12	125-145	135	20	3000-3400	3200	400
13	145-175	160	30	3400-3800	3600	400
14	175-225	200	50	3800-4200	4000	400
15	225-275	250	50	4200-4600	4400	400
16	275-325	300	50	4600-5000	4800	400
17	325-400	362.5	75	5000-6000	5500	1000
18	400-475	437.5	75	6000-7000	6500	1000
19	475-550	512.5	75	7000-8000	7500	1000
20	550-625	587.5	75	8000-9000	8500	1000
21	625-700	662.5	75	9000-10000	9500	1000
22	700-800	750	100	10000-12000	11000	2000
23	800-900	850	100	12000-14000	13000	2000
24	900-1000	950	100	14000-16000	15000	2000
25	1000-1200	1100	200	16000-18000	17000	2000
26	1200-1400	1300	200	18000-20000	19000	2000
27	1400-1600	1500	200	20000-25000	22500	5000
28	1600-1800	1700	200	25000-30000	27500	5000
29	1800-2000	1900	200			

To measure hydrometeor size, the "fastcircle" method fits the smallest possible circle around a hydrometeor image and uses the circle diameter as the hydrometeor diameter. The measured hydrometeor area dvided by the fast circle area is the area ratio, which gives an indication of the roundness of hydrometeors. Frozen hydrometeors are typically not round and have a low area ratio, while raindrops have a high area ratio. A perfect sphere would have an area ratio of 1.0; however, raindrops typically have an area ratio of 0.8 due to image stretching (Heymsfield et al. 2015). The area ratio of a hydrometeor depends in part on the resolution of the image. For spherical hydrometeors, a high resolution probe has a larger area ratio than a low resolution probe due to more pixels that more closely matches a perfect circle (Figure 2; Table 3). The area ratio is also impacted by variations in the imaged area and fast circle area due to the portion of the pixel that is shadowed (Figure 2). For the pixel to be counted as part of the hydrometeor image, the shadow depth must be 50 percent or greater in the pixel (Lawson et al. 2006). Thus, to determine which pixels are counted, the hydrometeor image is enclosed with the smallest circle that fully includes all pixels and any pixel with greater than 50 percent coverage of the circle is counted. Note that variability in the shape of raindrops (e.g., Gorgucci et al. 2006) or offsets in the hydrometeor position may cause variations in which pixels are counted for a round image, especially for lower resolution probes such as the HVPS3.

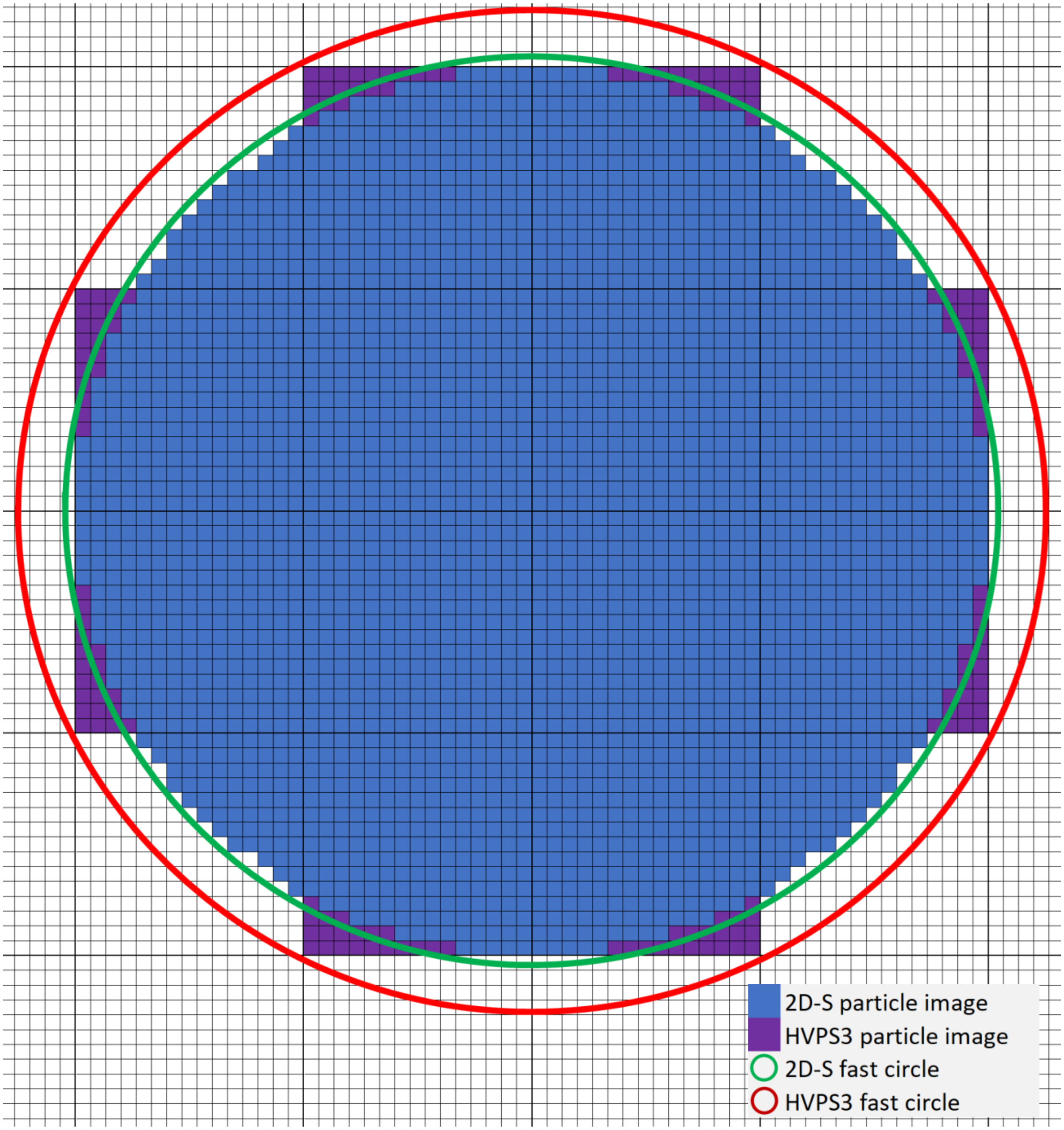

Figure 2: Figure showing area ratio configuration for a 600 µm circular hydrometeor as imaged by the Two-Dimensional Stereo (2D-S) Probe (thin grid) and the High Volume Precipitation Spectrometer Version 3 (HVPS3) (thick grid).

Table 3: Table showing the area ratio calculation for a 600 µm diameter hydrometeor imaged by the Two-Dimensional Stereo (2D-S) Probe (thin grid) and the High Volume Precipitation Spectrometer Version 3 (HVPS3) and depicted in Figure 2.

	2D-S	**HVPS3**
Image Size [μm^2]	282400	270000
Fast Circle [μm^2]	303054	368212

Area Ratio	**0.93**	**0.73**

Hydrometeors are rejected from processing when the area ratio is less than 0.1. Partially captured hydrometeors are processed using the "reconstruction" method in which hydrometeors that touch the edge of the imaging array are recreated using the algorithm described by Heymsfield and Parrish (1978). The "reconstruction" method results in an effectively larger sample volume for the probes by including hydrometeors that do not fully fit in the imaging array and has the largest effect on the 2D-S due to its lower sample volume. When large hydrometeor imaging probes such as the HVPS3 are used in combination with the 2D-S, the "centerin" method has typically been used (e.g., Wagner and Delene 2022). The "centerin" method rejects hydrometeors if their center of mass is outside the imaging array. However, the "centerin" method has a higher concentration of hydrometeors, likely due to the lower effective sample volume with this method (Heymsfield and Parrish 1978). Because of the larger effective sample volume, the "reconstruction" method is used to process the HVPS3 data.

2.4 Ice-bulb and Wet-bulb Temperature

The newly developed ADPAA module, bulbtemp, uses air temperature, dew point temperature, and pressure to calculate the web-bulb and ice-bulb temperature. The difference between the wet-bulb and ice-bulb temperature is larger at lower pressure and relative humidity (Figure 3). At 100 percent relative humidity, the ice-bulb, wet-bulb, and air temperature are all equal. Below 100 percent relative humidity, both the ice-bulb and wet-bulb temperature are less than the air temperature, and the ice-bulb is always less than the wet-bulb. For decreasing relative humidity, the wet-bulb and ice-bulb temperature continue to decrease relative to the air temperature. At 2 °C air temperature, the ice-bulb temperature is 0 °C at approximately 80 percent relative humidity for a pressure of 1,000 hPa, whereas the ice-bulb temperature is 0 °C at approximately 75 percent relative humidity for a pressure of 500 hPa. Additional details on the bulbtemp module and the calculations are provided in Appendix A and Table A1.

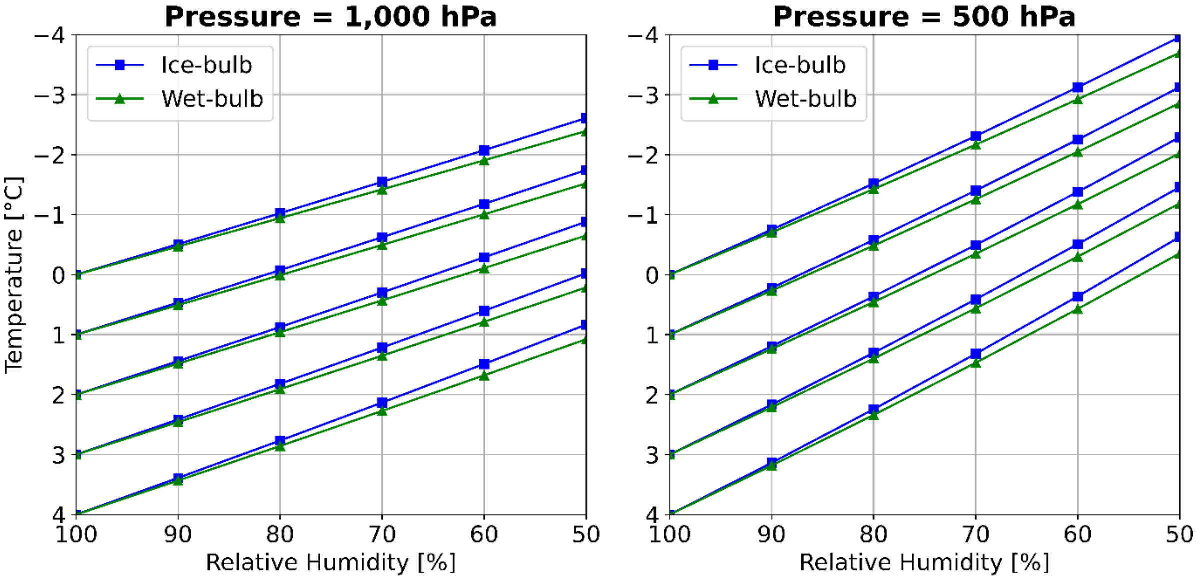

Figure 3: The ice-bulb temperature compared to wet-bulb temperature for varying air temperatures as a function of relative humidity at 500 hPa (left) and 1,000 hPa (right). The air temperature used to calculate the bulb temperatures uses integer values ranging from 0 °C to 4 °C at 1 °C intervals (top to bottom line series in each plot).

The 0 °C ice-bulb temperature is used to define the top of the melting layer (Figure 4). Hydrometeors in an environment with an air temperature is above 0 °C and the ice-bulb temperature below 0 °C will sublimate (colored in blue in Figure 4). With increasing relative humidity, the air temperature at the 0 °C ice-bulb isotherm decreases. In dry conditions as low as 20 percent relative humidity at 500 hPa, snow will continue to sublimate until almost 10 °C. Conversely, at 1,000 hPa and 20 percent relative humidity, snow will sublimate until almost 6 °C.

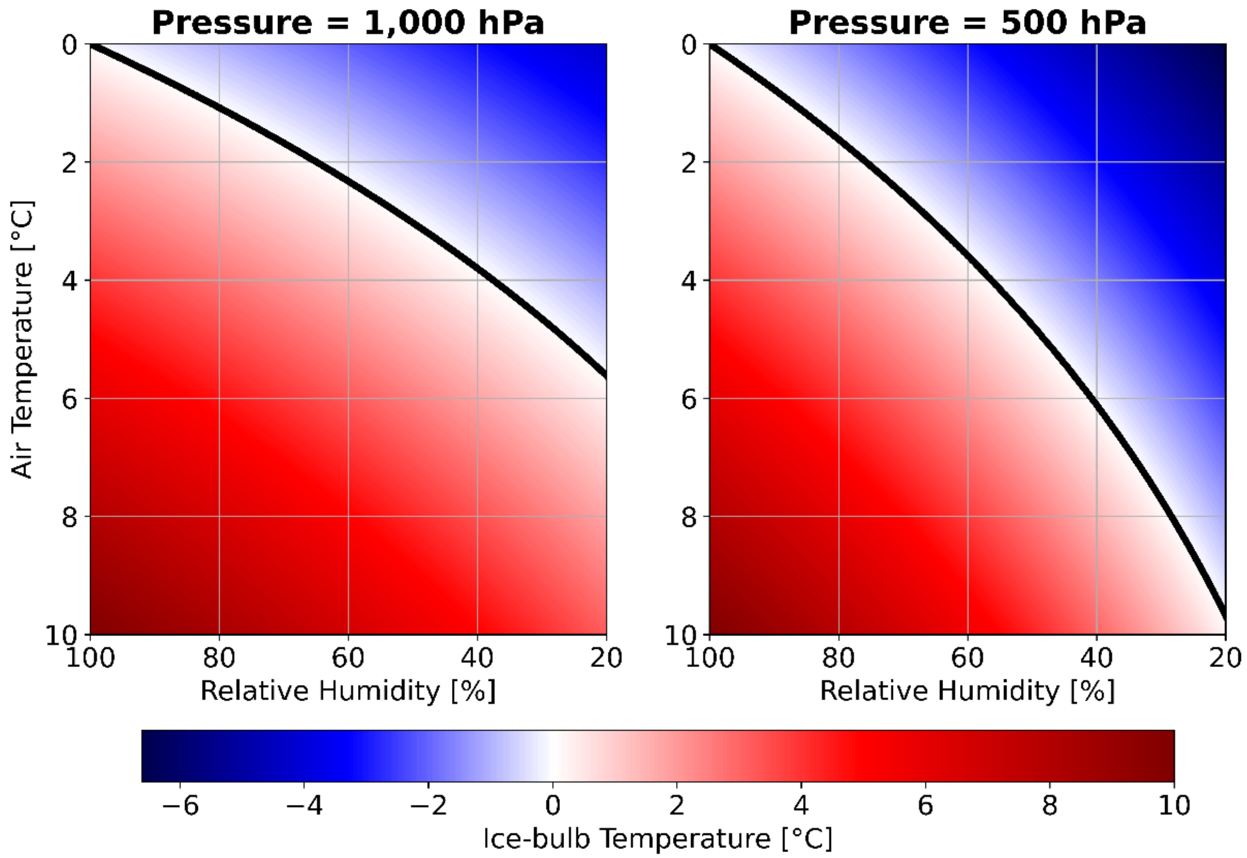

Figure 4: The 0 °C ice-bulb isotherm (black line) at 1,000 hPa (left) and 500 hPa (right).

CHAPTER 3

METHODOLOGY

A melting layer profile is obtained by a continuous vertical measurement of hydrometeors that undergo melting. Melting layer profiles are restricted to in-situ sampling during aircraft ascents and descents to eliminate horizontal sampling of hydrometeors that appear to transition in phase even though is no vertical layer of melting. Additionally, restricting melting layer profiles to ascents and descents reduces sampling of horizontal cloud variability. Potential melting layer profiles are determined for each aircraft flight by reviewing microphysics and thermodynamic probe measurements. A total hydrometeor concentration of 10^3 #/m^{-4} measured by optical array probes is the minimum in-cloud threshold throughout the melting layer.

The melting layer depth is the vertical distance between the 0 °C ice-bulb isotherm and the altitude where all hydrometeors are fully melted. Hydrometeors sublimate in regions where the air temperature is above 0 °C and the ice-bulb temperature is below 0 °C, while hydrometeor melt where both the air temperature and ice-bulb temperature are above 0 °C (Figure 4). Hydrometeor images from optical array probes do not show the details necessary to determine if hydrometeors are starting to melt at the melting layer top. However, optical array probe images can be used to determine the melting layer bottom. The “melted” location is when the hydrometeor images first indicate fully rounded hydrometeors with no jagged edges. As noted by Heymsfield et al. (2021), manually identifying fully melted hydrometeors is preferred as an automated hydrometeor detection method may result in error as the distinguishing factors between melted and non-melted hydrometeors are somewhat arbitrary. Manual identification is still inherent uncertainty as laboratory experiments indicated that ice may be contained within a round drop (e.g., Matsuo and Sasyo 1981). Heymsfield et al. (2021) indicated that area ratio obtained from probe images is a potential identifier of melted hydrometeor; therefore, area ratio is compared to manual identification to determine consistency in identifying the melting layer bottom.

Figure 5 shows an example profile of a melting layer that fulfills all the melting layer criteria. The aircraft descended through increasing temperature near the 0 °C isotherm and had HVPS3 probe concentrations above 10^3 #/m^{-4} for the entire profile. The ice-bulb temperature exceeds 0 °C, indicating melting. Additionally, the profile of the ice-bulb temperature is very similar to that of the air temperature, suggesting that the environment is saturated with the relative humidity at or near 100 percent for the majority of the descent. Flights from several field campaigns (Table 1) are similarly scrutinized to identify potential melting layers.

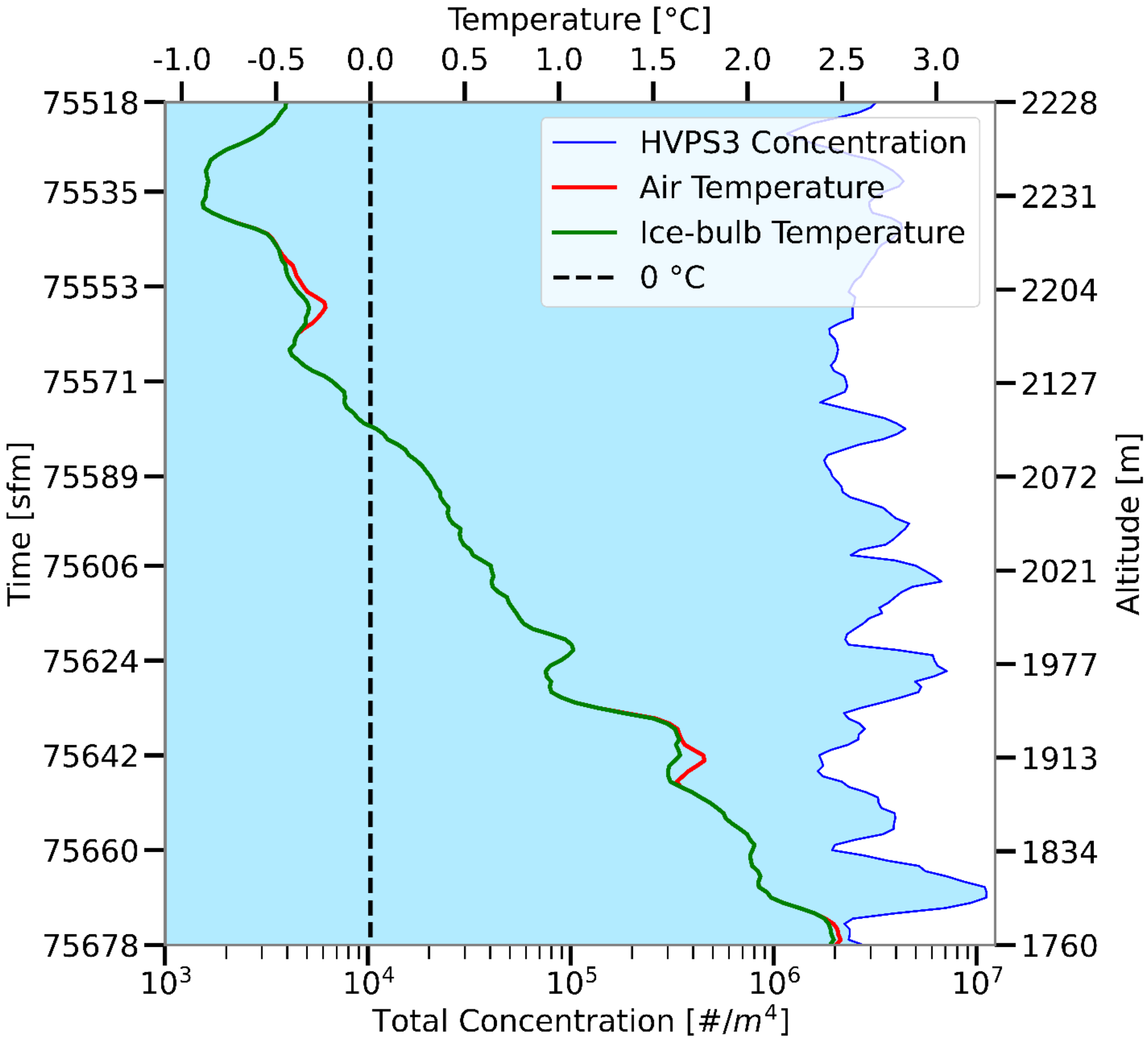

Figure 5: Plot detailing a melting layer profile from 12 NOV 15 during the OLYMPEX field campaign. The total concentration (bottom x-axis) is summed for all channels of the HVPS3 probe, shown in the filled contour. Time is shown in seconds from midnight (sfm). Data are averaged every five seconds to smooth out spikes.

Using the potential melting layer profiles, optical array probe images are analyzed to confirm that hydrometeors undergo melting. Hydrometeor images are inspected for a transition from frozen to liquid hydrometeors. The larger sampling volume of the HVPS3 provides more hydrometeor images; however, the higher resolution of the 2D-S (or 2D-C for earlier field campaigns when the 2D-S is unavailable) provides more detailed images, which increases the accuracy of qualitatively determining when all hydrometeors are melted. Figure 6 shows example HVPS3 and 2DS probe images within the melting layer where there is a clear transition from frozen to liquid hydrometeors with mixed hydrometeors in between. With its larger sample volume, the HVPS3 provides more images of larger diameter hydrometeors above, within, and below the melting layer (Figure 6a). However, detailed characteristics of the hydrometeors can be hard to depict due to the low resolution of the HVPS3, which uses 150 μm diodes. The low resolution becomes especially important as hydrometeors become round and more difficult to identify features differentiating between partially or fully melted hydrometeors. The 2D-S provides a higher resolution look at hydrometeors and their habits at the cost of a lower sample volume and fewer hydrometeors sampled (Figure 6b). In mixed-phased clouds, the HVPS3 images appear more round, but lack the detail given by the 2D-S images. The 2D-S shows only a single melting aggregate in the image array, but captures features necessary to identify it as a mixed hydrometeor. For fully melted hydrometeors, the raindrops only encompass a few pixels in the HVPS3 (Figure 6a), while the 2D-S gives a clear visual of hydrometeor roundness (Figure 6b). When used in conjunction, the HVPS3 and 2D-S give a complete picture for identifying the melting layer bottom.

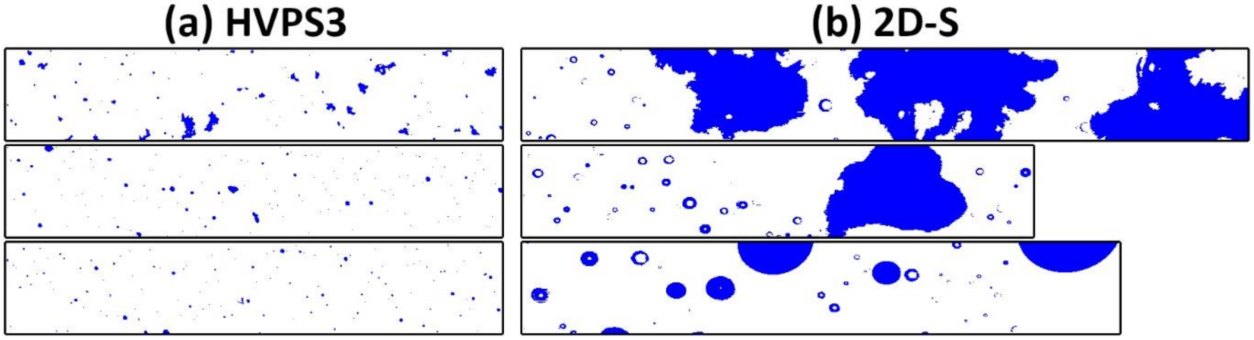

Figure 6: Images from the (a) High Volume Precipitation Spectrometer Version 3 (HVPS3) probe and (b) Two Dimensional Stereo (2D-S) probe depicting the transition from frozen to liquid hydrometeors during a melting layer penetration on 12 NOV 15 during OLYMPEX. The images from the two probes are taken at the same time in seconds from midnight (sfm), showing three stages of hydrometeors: 1) frozen hydrometeors (top; 75571 sfm); 2) mixed hydrometeors (middle; 75586 sfm); 3) liquid hydrometeors (bottom; 75628 sfm). Each image is 128 pixels tall with a pixel resolution of 150 μm for the HVPS3 and 10 μm for the 2D-S.

Three-dimensional visualization of the aircraft flight path through the melting layer (Figure 7) is used to determine penetration type. While spiral ascents and descents included both Lagrangian and Eulerian spirals (eg., Heymsfield et al. 2015, 2021), it is difficult to distinguish between the two types of spirals. Therefore, the penetration type when the aircraft turns while profiling the melting layer is considered a spiral (Figure 7a). Ramps are flight paths that do not spiral as the aircraft ascends or descends while moving horizontally (Figure 7b).

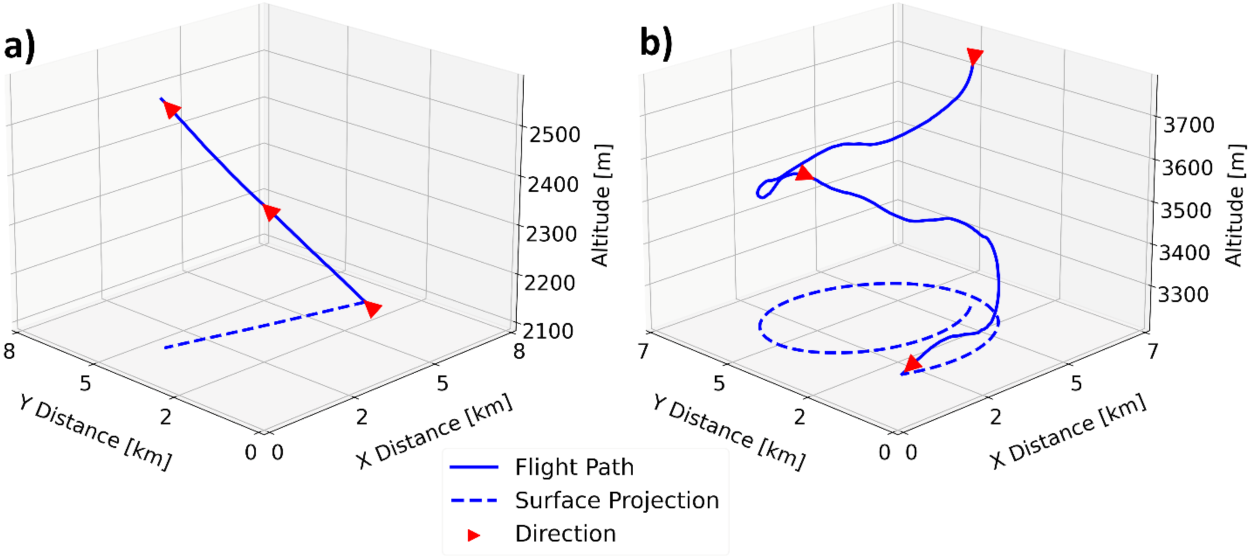

Figure 7: Plots showing the melting layer penetration types: (a) ramp ascent on 12 NOV 2015 during OLYMPEX and (b) spiral descent on 11 MAY 10 during MC3E. The altitude of the flight path (solid blue line) and its surface projection (dashed blue line) is from the 0 °C isotherm to the melting layer bottom. The X Distance shown is latitudinal distance and the Y Distance is longitudinal distance.

Optical array probe measurements above, within, and below the melting layer are analyzed to determine differences in hydrometeor concentration and area ratio, and how relative humidity affects these parameters. Additionally, the 0 °C ice-bulb and air temperature are compared for defining the melting layer top. Typically, measurements from a small sized hydrometeor probes, such as the 2D-S, are combined with measurements from a large sized hydrometeor probes, such as the HVPS3, to create a full hydrometeor spectrum for analysis (e.g., Heymsfield et al. 2015; Wagner and Delene 2022). The combined spectrum has some diameter, such as 1,000 µm, that separates measurements from the two probes (Table 2). Combining the probe measurements provides a continuous size distribution with the high size resolution of the 2D-S and the large sampling volume of the HVPS3. However, with the 1 Hz spectrum, the 2D-S probe's small sample volume results in zero hydrometeor counts in the 300-2,000 μm size range, using "standard" channel spacing (Table 2), while the HVPS3 captures many particles of that size (Figure 8). The low hydrometeor counts impact the uncertainty of the area ratio. Thus, to enable use of the 1 Hz spectrum and the standard channel spacing, only the HVPS3 probe is used to create the spectrum for the melting layer analysis. Longer time periods can be used to create the hydrometeor spectra; however, vertical resolution would be compromised, so the accuracy of determining the melting layer bottom using area ratio would be reduced (Figure 9). Additionally, the longer time periods do not improve long periods of zero hydrometeor counts. Hydrometeor melting is also expected to have the most significant effect on larger hydrometeors (e.g., Heymsfield et al. 2015), which the 2D-S does not measure. Therefore, the analysis spectrum only uses HVPS3 measurements. The 2D-S and other small hydrometeor probes are still used to analyze images to determine the extent of melting in identified melting layers.

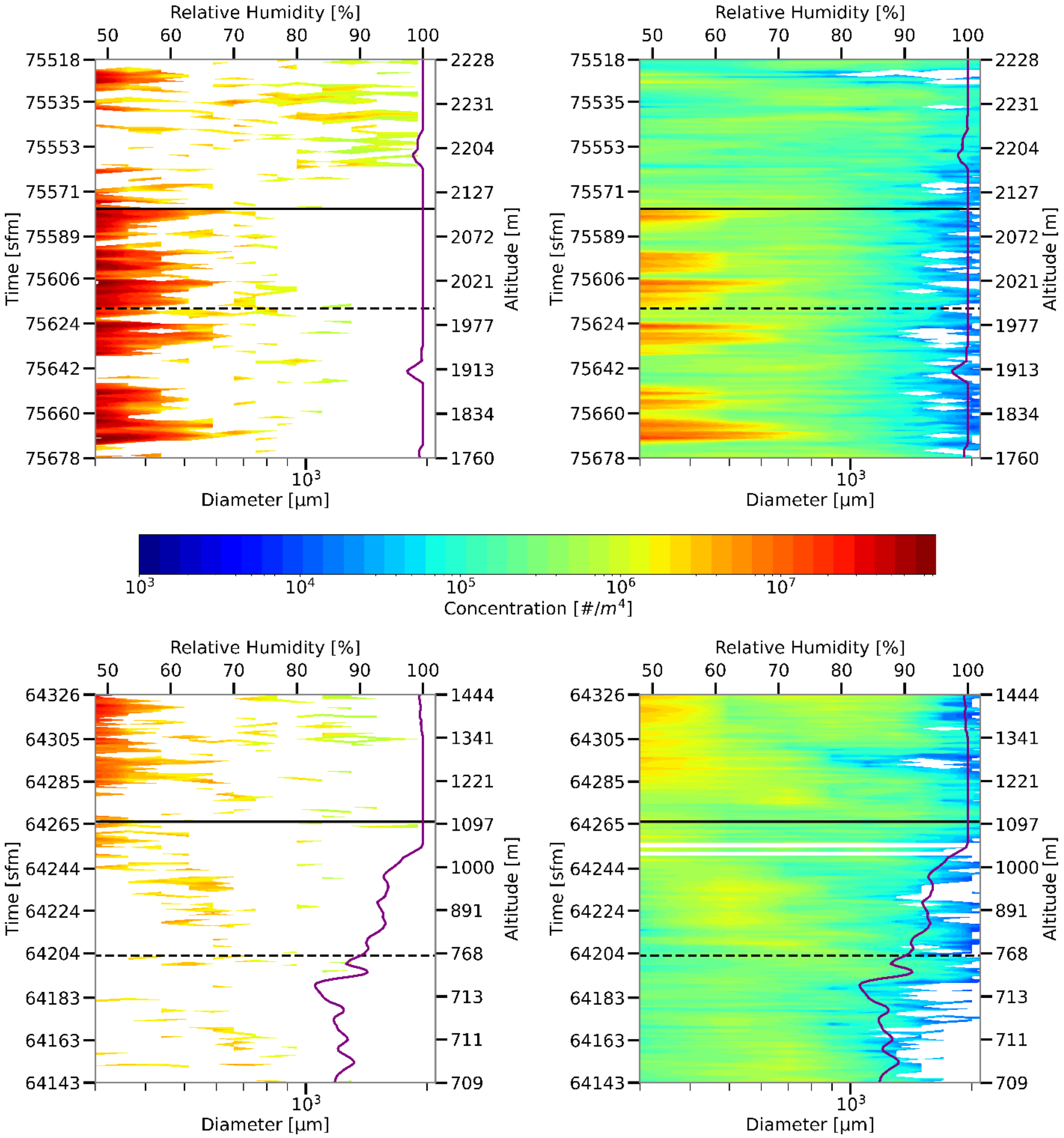

Figure 8: Plots showing melting layer changes in the hydrometeor size distribution for the Two-Dimensional Stereo (2D-S) probe (left) and the High Volume Precipitation Spectrum Version 3 (HVPS3) probe (right) for two cases: 12 NOV 2015 (top) and 12 DEC 2015 (bottom) during OLYMPEX. The horizontal solid black line depicts the melting layer top and dashed black line depicts the melting layer bottom. Relative humidity (purple line) is averaged every 5 s. Channel sizes used in the spectrum are given in Table 2.

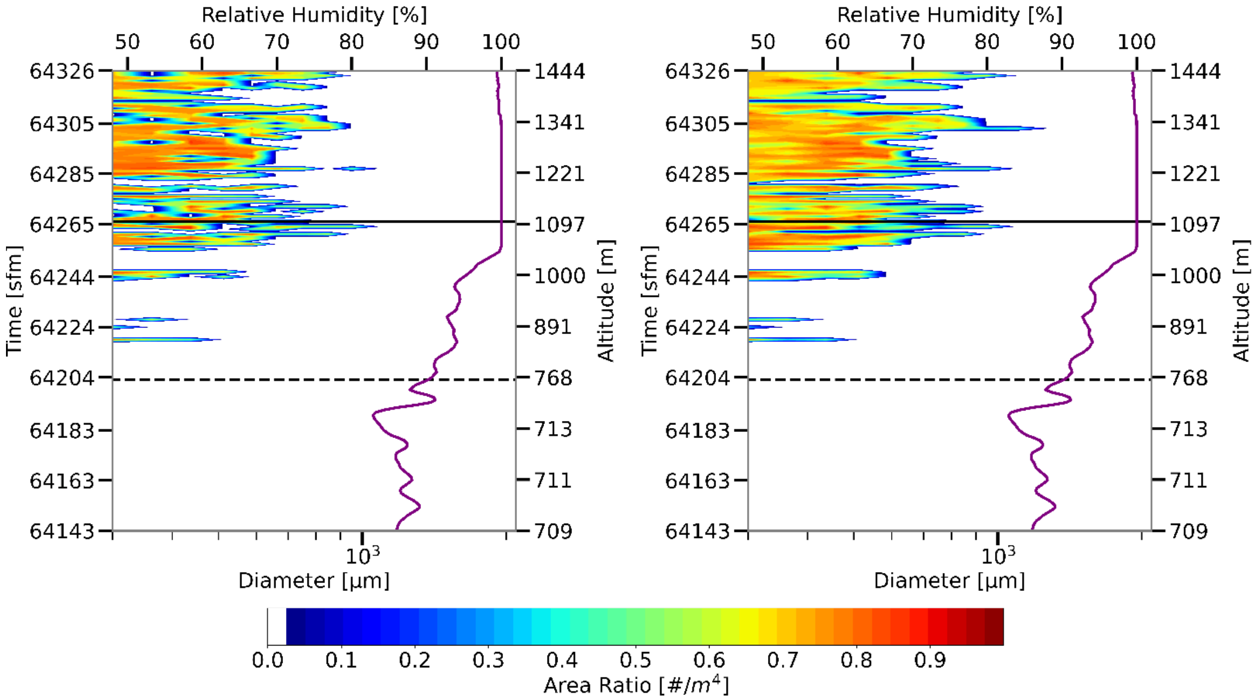

Figure 9: Plot showing area ratio measurements from the Two-Dimensional Stereo (2D-S) probe 1 s spectrum (left) and 5 s spectrum (right) for the 12 DEC 2015 case. The horizontal solid black line depicts the melting layer top and dashed black line depicts the melting layer bottom. Relative humidity (purple line) is averaged every 5 s. Channel sizes used in the spectrum are given in Table 2.

For useful area ratio analysis, channels need a sufficient number of pixels since channels that encompass only one or two pixels of hydrometeors would have erroneously high area ratio values, similar to that of spherical drops, even if the hydrometeors are frozen. Figure 10 shows that above the melting layer, the HVPS3 has a larger area ratio at 300 µm than the 2D-S; however, slightly smaller area ratio values at larger diameters. Therefore, HVPS area ratio analysis is conducted starting at 500 µm.

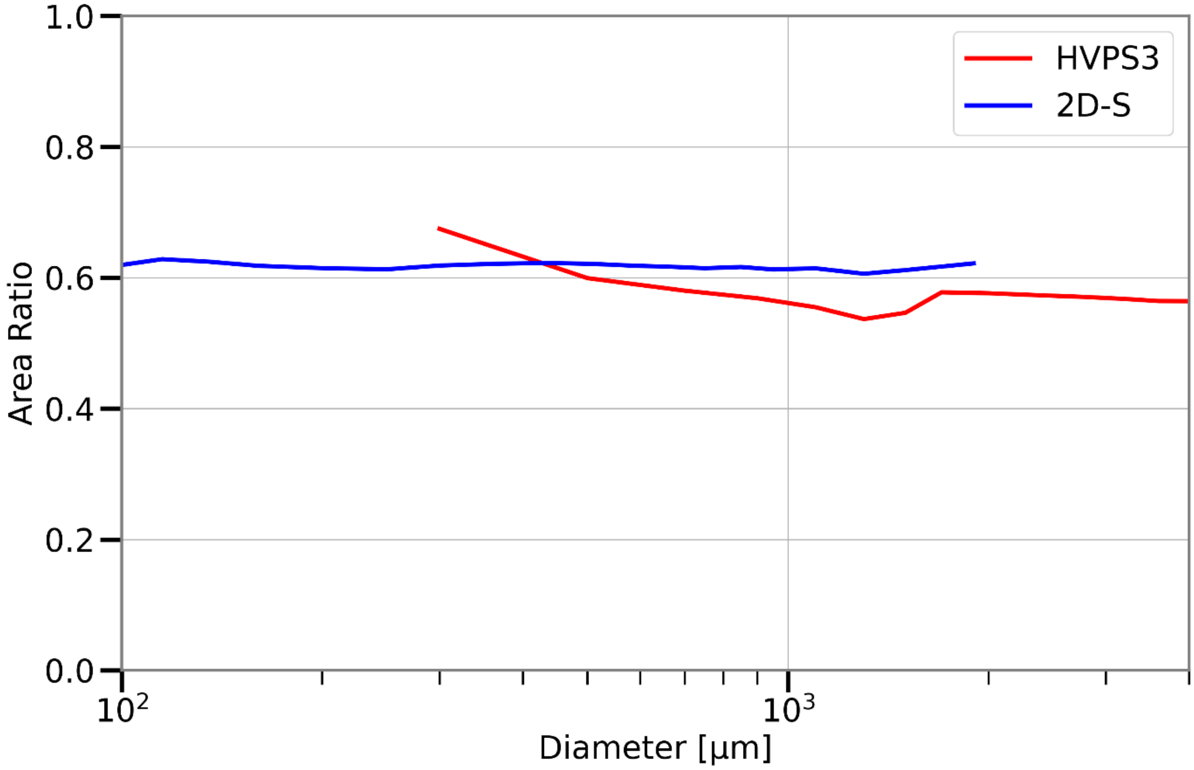

Figure 10: Plot showing area ratio measurements for the Two-Dimensional Stereo (2D-S) probe (blue) and the High Volume Precipitation Spectrum Version 3 (red) on 12 DEC 15 during OLYMPEX field project. The time period from 64,266 seconds from midnight (sfm) to 69,266 sfm is used to give 83 min and 20 s of measurements above the melting layer. Channel sizes used in the spectrum are given in Table 2.

The HVPS3 hydrometeor size distribution is fitted to an exponential distribution (1) from 200 μm to 30,000 μm. The intercept and slope parameters are calculated using the SciPy module's curve_fit function, which uses the method of least squares to minimize the residuals. To improve computation time and accuracy, an initial guess of $N_0 = 8 \times 10^6$ m^{-4} for the intercept parameter and $\lambda = 2$ mm^{-1} for the slope parameter are used. However, tests confirmed that the initial guess does not alter the results. Spectrum duration and channel sizes change concentration and area ratio values; therefore, the analysis is on trends through the melting layer and how they change rather than the specific magnitude of values. The hydrometeor spectrum is analyzed with the Python programming language (version 3) and the ADPAA module. The ADPAA program Aplot is used to quickly visualize data and identify potential melting layer profiles. The ADPAA Python object is used to import all data and the Matplotlib Python module is used for visualization.

CHAPTER 4

RESULTS

4.1 Characteristics of Melting Layer Penetrations

From five field campaigns (Table 1), a total of thirty-three melting layer cases are identified with fifteen ramps and eighteen spirals (Table 4). Most of the cases occur in high relative humidity conditions with six being saturated throughout the entire melting layer depth, seventeen cases having an average relative humidity > 90 percent, and night have less than 85 percent. There is no pattern between penetration type and relative humidity.

Table 4: Matrix showing the number of melting layer profiles by type of aircraft flight provide and average relative humidity (RH) environment throughout the melting layer. Low RH is 90 percent and less, high RH is greater than 90 percent, and saturated is 100 percent throughout the entire melting layer depth.

	Low (≤ 90%) RH	**High (> 90%) RH**	**Saturated**	**Total**
Spiral	4	8	6	18
Ramp	5	9	1	15
Total	**9**	**17**	**7**	**33**

The aircraft profile sampling characteristics and melting layer relative humidity are given in Table 5. Six of the nine low relative humidity cases are from MC3E, which had the lowest (63 percent) relative humidity. All five melting layers from GCPEX are during a single flight; however, the profile type and relative humidity varied, as well as the depth of the melting layer. The two IPHEX melting layers have similar depths at approximately 336 m and 347 m, while the melting layer relative humidity is 100 percent and 92 percent, respectively. OLYMPEX has the most cases with fifteen profiles from ten flights. Nine of the fifteen OLYMPEX profiles are ramps. Additionally, OLYMPEX has some of the shallowest melting layer depths, as little as 65 m. The relative humidity is typically high during OLYMPEX with relative humidity being above 90 percent for all but one melting layer, and a relative humidity across all cases of 96.4 percent.

Finally, IMPACTS saw two deep melting layers, both near 500 m deep and relative humidity near 95 percent.

Table 5: Table showing a summary of the melting layer aircraft observations where the case name is based on the field campaign, profile type, and relative humidity (RH). Cases are listed in descending relative humidity order with row shading for three relative humidity ranges: saturated, greater than 90 percent, and 90 percent or less.

Case Label *Project_Profile_RH*	**Date** *YYYYMMDD*	**Start** *sfm*	**Length** *s*	**Depth** *m*	**Profile Type**		**RH** *%*
OLYMPEX_Spi-Des_100RHa	20151023	57664	22	83	Spiral	Descent	100
OLYMPEX_Ram-Des_100RH	20151112	75578	40	107	Ramp	Descent	100
OLYMPEX_Spi-Des_100RHb	20151123	79641	21	120	Spiral	Descent	100
OLYMPEX_Spi-Des_100RHc	20151218	23006	34	194	Spiral	Descent	100
GCPEX_Spi-Asc_100RH	20120127	17666	170	563	Spiral	Ascent	100
IPHEX_Spi-Asc_100RH	20140509	68961	80	336	Spiral	Ascent	100
GCPEX_Spi-Asc_99RH	20120127	16904	75	395	Spiral	Ascent	99
OLYMPEX_Spi-Asc_99RHa	20151123	80111	39	117	Spiral	Ascent	99
OLYMPEX_Ram-Des_99RH	20151201	84256	45	181	Ramp	Descent	99
OLYMPEX_Spi-Asc_99RHb	20151201	85421	41	284	Spiral	Ascent	99
MC3E_Spi-Asc_99RH	20110427	38313	82	436	Spiral	Ascent	99
OLYMPEX_Ram-Des_98RHa	20151212	63412	58	251	Ramp	Descent	98
OLYMPEX_Spi-Asc_98RH	20151112	77802	48	271	Spiral	Ascent	98
OLYMPEX_Ram-Des_98RHb	20151213	83737	23	108	Ramp	Descent	98
GCPEX_Spi-Asc_97RH	20120127	11926	42	453	Spiral	Ascent	97
OLYMPEX_Ram-Des_96RH	20151112	80832	41	291	Ramp	Descent	96
IMPACTS_Ram-Asc_95RH	20200220	87676	86	519	Ramp	Ascent	95
OLYMPEX_Ram-Asc_95RH	20151212	64265	62	334	Ramp	Ascent	95
MC3E_Spi-Des_95RH	20110427	36454	106	458	Spiral	Descent	95
MC3E_Spi-Des_95RH	20110520	55073	71	424	Spiral	Descent	95
IMPACTS_Spi-Des_94RH	20200205	80842	106	494	Spiral	Descent	94
IPHEX_Ram-Asc_92RH	20140527	77277	42	347	Ramp	Ascent	92
OLYMPEX_Ram-Asc_92RH	20151118	84662	68	341	Ramp	Ascent	92
OLYMPEX_Ram-Des_91RH	20151114	77738	15	65	Ramp	Descent	91
MC3E_Spi-Asc_90RH	20110520	48744	84	525	Spiral	Ascent	90
GCPEX_Spi-Des_84RH	20120127	10827	60	179	Spiral	Descent	84
MC3E_Ram-Asc_83RHa	20110510	84287	73	402	Ramp	Ascent	83
MC3E_Ram-Asc_83RHb	20110510	85126	40	124	Ramp	Ascent	83
OLYMPEX_Ram-Asc_82RH	20151113	54743	55	505	Ramp	Ascent	82
MC3E_Ram-Des_79RH	20110510	85034	49	133	Ramp	Descent	79
MC3E_Spi-Des_75RH	20110520	59542	62	311	Spiral	Descent	75
GCPEX_Ram-Des_71RH	20120127	19188	38	295	Ramp	Descent	71
MC3E_Spi-Des_63RH	20110510	82885	113	383	Spiral	Descent	63

4.2 Saturated Melting Layers

The OLYMPEX_Ram_Des_100RH case is representative of the seven 100 percent relative humidity cases with no quasi-isothermal layer near the melting layer top (Figure 5). The hydrometeor concentrations are relatively high above the melting layer top, while the area ratio is small (< 0.5) for hydrometeor above 400 µm (Figure 11). Interestingly, the area ratio of smaller hydrometeors starts to increase just above the melting layer, which is not expected until just after melting begins. There is an increase in maximum hydrometeor diameter at 5,000 µm approximately 30 m below the melting layer top, in which hydrometeors 1,100 µm and larger have a smaller area ratio of 0.6 and lower. The low area ratio suggests that the larger hydrometeors in the melting layer are not very round. By approximately 50 m below the melting layer top, area ratio increases for the larger hydrometeors to 0.8 and the maximum diameter decreases to 3,000 µm. Below the melting layer bottom, area ratio is consistently high for hydrometeors as they are round.

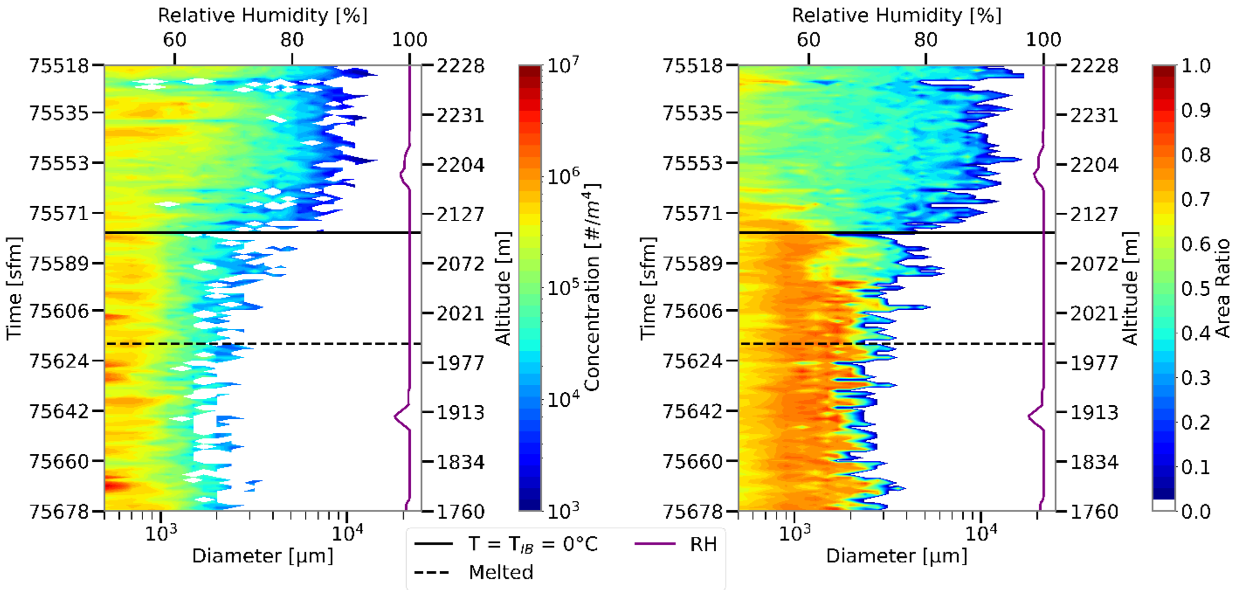

Figure 11: Plots showing hydrometeor concentration (left) and area ratio (right) through the melting layer during the OLYMPEX_Ram_Des_100RH case (Table 5). The High Volume Precipitation Spectrometer Version 3 (HVPS3) probe measurements are from 1 s spectra, whereas measurements of relative humidity with respect to water (RH) are 5 s averages. Horizontal black

lines depict the time and altitude of the 0 °C air temperature (T) isotherm, melting layer top at the 0 °C ice-bulb temperature (T_{IB}) isotherm, and the melting layer bottom where all hydrometeors are 'melted'. Altitude is shown on the right y-axis that corresponds with every time tick on the left y-axis. Concentration (left) is colored on a logarithmic scale, while area ratio (right) is colored on a linear scale. Hydrometeor diameter on the bottom x-axis is plotted on a logarithmic scale, based on the HVPS3 bins defined in Table 2.

The exponential fit of the HVPS3 size distribution for OLYMPEX_Ram_Des_100RH (Figure 12) has three peaks in both fit parameters: one just above the melting layer bottom, one just below the melting layer bottom, and a final one about 200 m below the melting layer bottom. These spikes are due to a couple orders of magnitude increase in hydrometeor concentration for hydrometeors around 400 µm to 600 µm (Figure 11), which greatly influences both parameters. Neglecting the spikes, both parameters are smallest above the melting layer and largest below the melting layer. The parameters are only slightly smaller in the melting layer compared to below, as there is a rapid transition at the melting layer to the top where maximum diameter decreases.

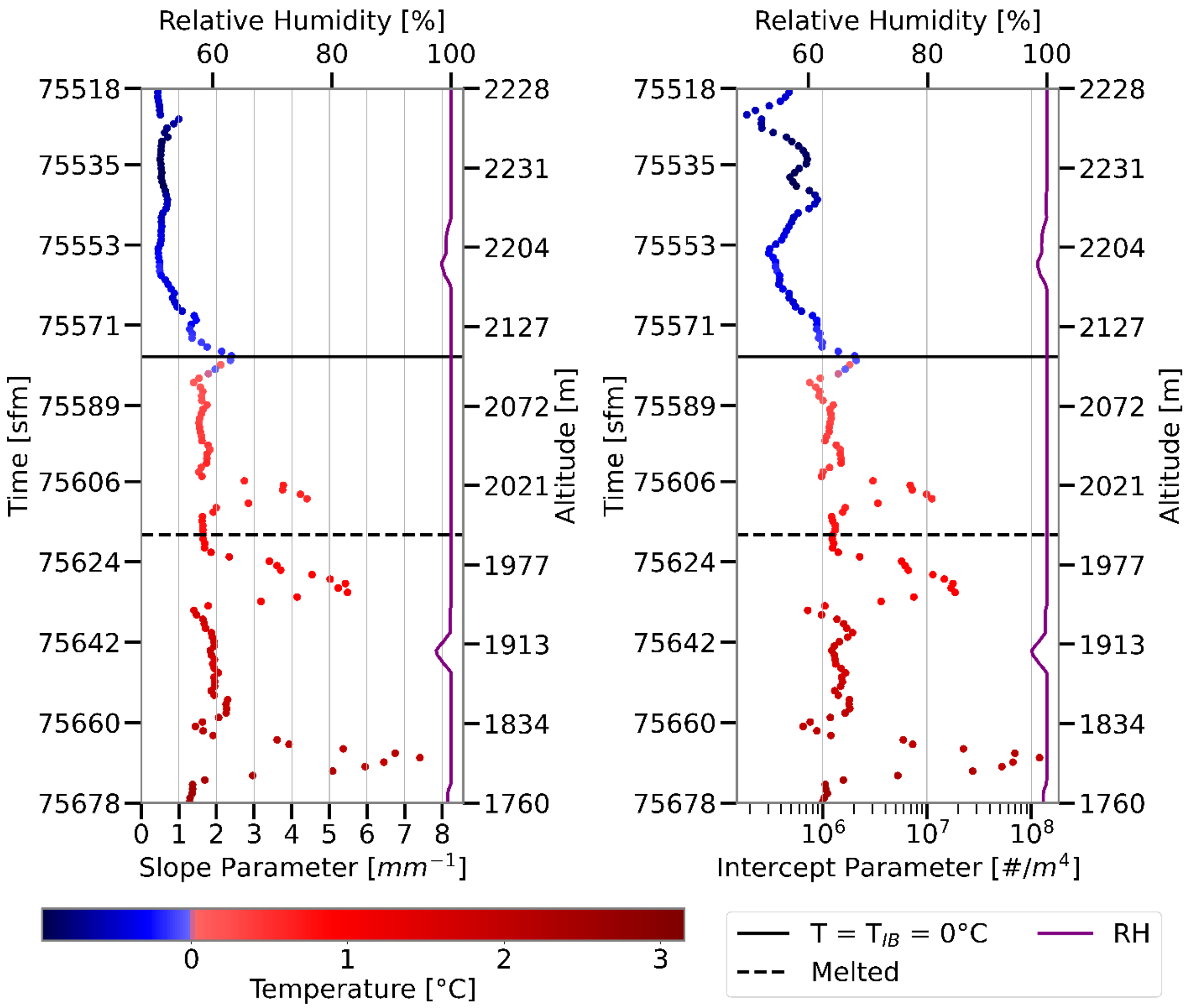

Figure 12: Plots showing the hydrometeor spectrum through the melting layer. The exponential fit of the slope parameter (left) and intercept parameter (right) are from 5 s averages of the 1 s spectrum from the High Volume Precipitation Spectrometer Version 3 (HVPS3) probe during the OLYMPEX_Ram_Des_100RH case (Table 5). Relative humidity with respect to water (RH) data are 5 s averages. Horizontal black lines depict the time and altitude of the 0 °C air temperature (T) isotherm, melting layer top at the 0 °C ice-bulb temperature (T_{IB}) isotherm, and the melting layer bottom where all hydrometeors are 'melted'

The area ratio in the OLYMPEX_Spi_Des_100RHb, OLYMPEX_Spi_Des_100RHc, and GCPEX_Spi-Asc_100RH cases change similarly to OLYMPEX_Ram_Des_100RH. Although, GCPEX_Spi-Asc_100RH is much deeper and the transition to higher area ratio is much slower (Figure 13). The OLYMPEX_Spi_Des_100RHa case differs from the other saturated cases (Figure 14) in having a lower area ratio values; however, the area ratio of the largest hydrometeors still increases as hydrometeors melt (Figure 14). Thus, area ratio values alone may not be an indicator for the melting layer bottom; rather, an increase in area ratio for the largest hydrometeors is necessary. Unexpectedly, the area ratio of hydrometeors smaller than 1,000 µm decreases by approximately 0.1 starting 50 m above the melting layer top instead of increasing. Following a decrease in maximum diameter at the melting layer top, maximum diameter increases from approximately 2,500 µm to 4,000 µm over a 50 m depth in the middle of the melting layer.

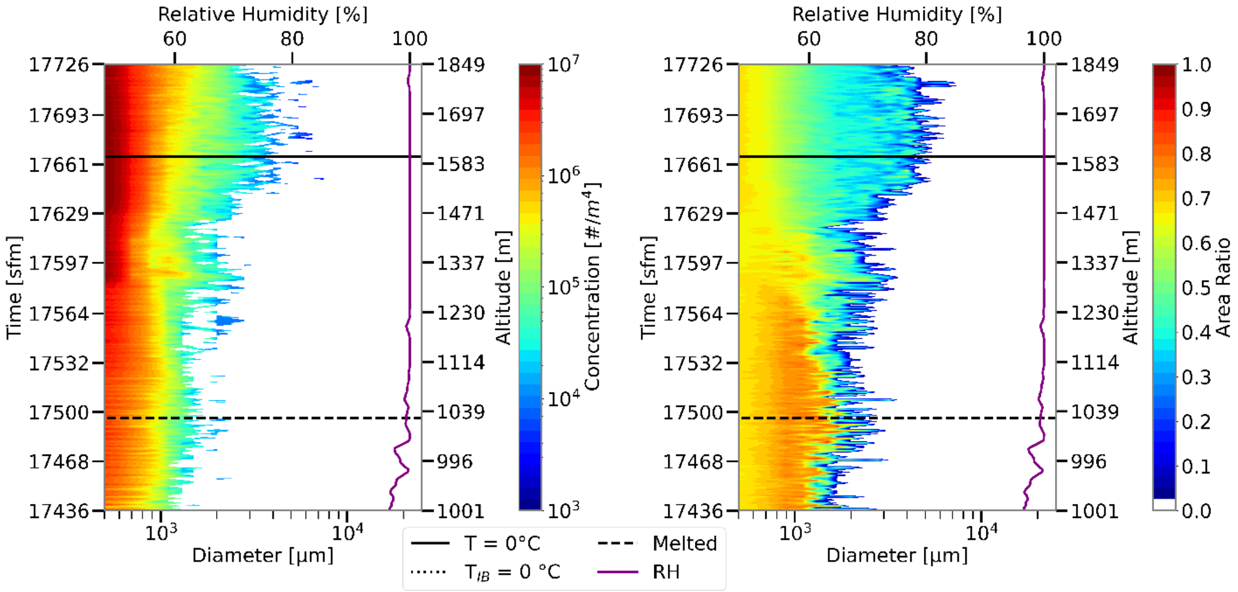

Figure 13: Plots similar to Figure 11, except for showing the melting layer for the GCPEX_Spi-Asc_100RH case (Table 5).

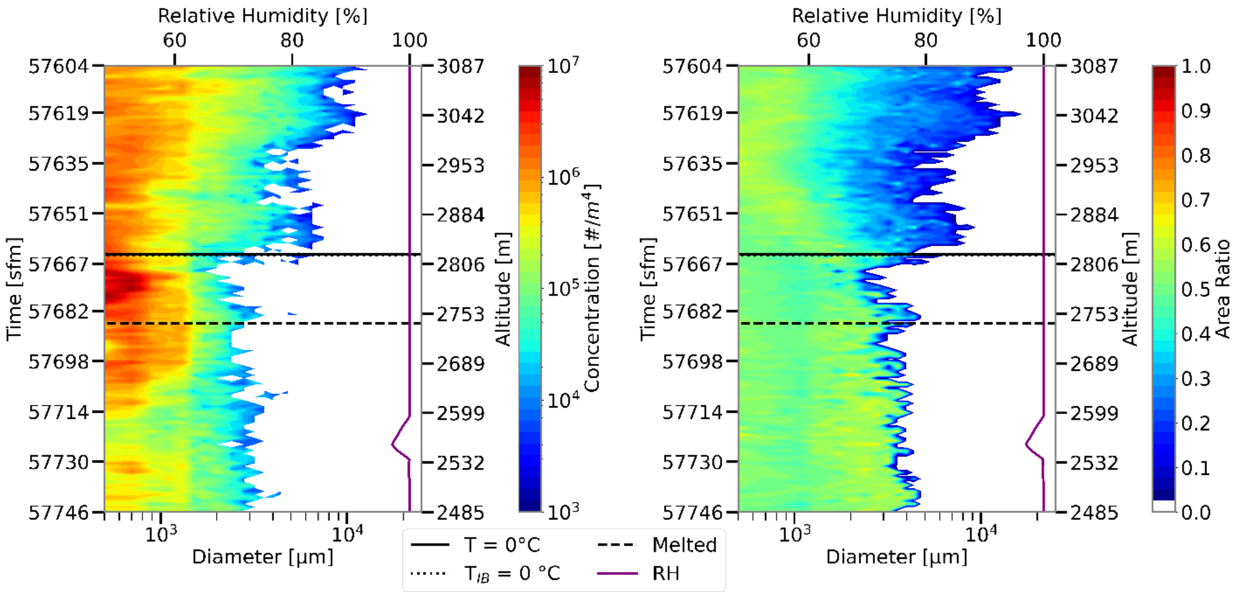

Figure 14: Plots similar to Figure 11, except for showing the melting layer for the OLYMPEX_Spi-Des_100RHa case (Table 5).

The intercept and slope parameters from the exponentially fitted size distribution vary greatly between the saturated cases. Contrasting OLYMPEX_Ram_Des_100RH, both parameter trends downward in the melting layer during OLYMPEX_Spi-Des_100RHc (Figure 15). During GCPEX_Spi-Asc_100RH, both parameters slowly increase from above the melting layer to approximately 200 m below the melting layer top (Figure 16). There is a peak in the parameters associated with slightly increased hydrometeor concentrations in the middle of the melting layer (Figure 13). In the lowest 250 m of the melting layer, both parameters decrease towards the melting layer bottom where they roughly level off (Figure 16). Ultimately, both parameters are lower below the melting layer than above (Figure 16).

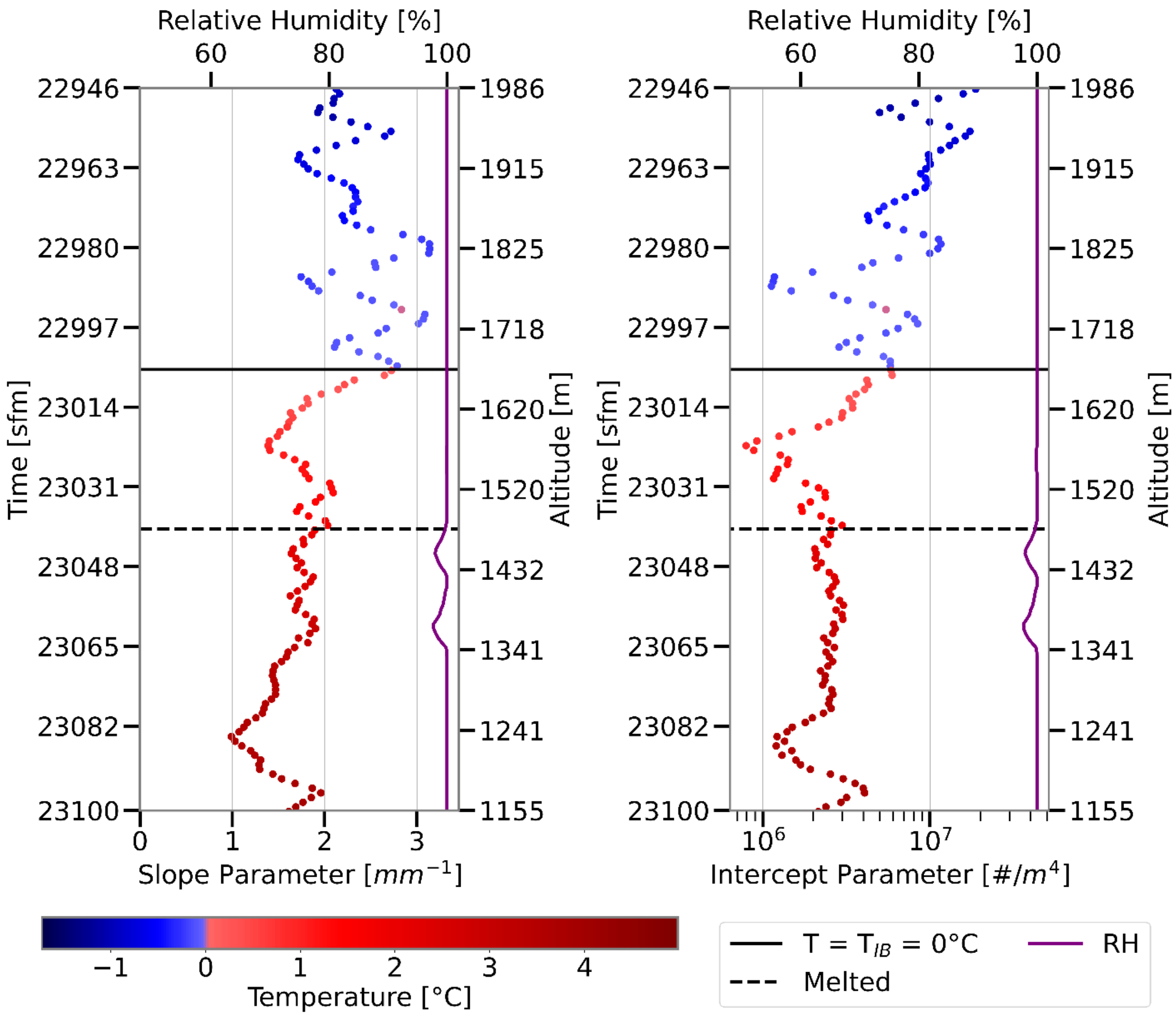

Figure 15: Plots similar to Figure 12, except for showing the melting layer for the OLYMPEX_Ram-Des_98RHb case (Table 5).

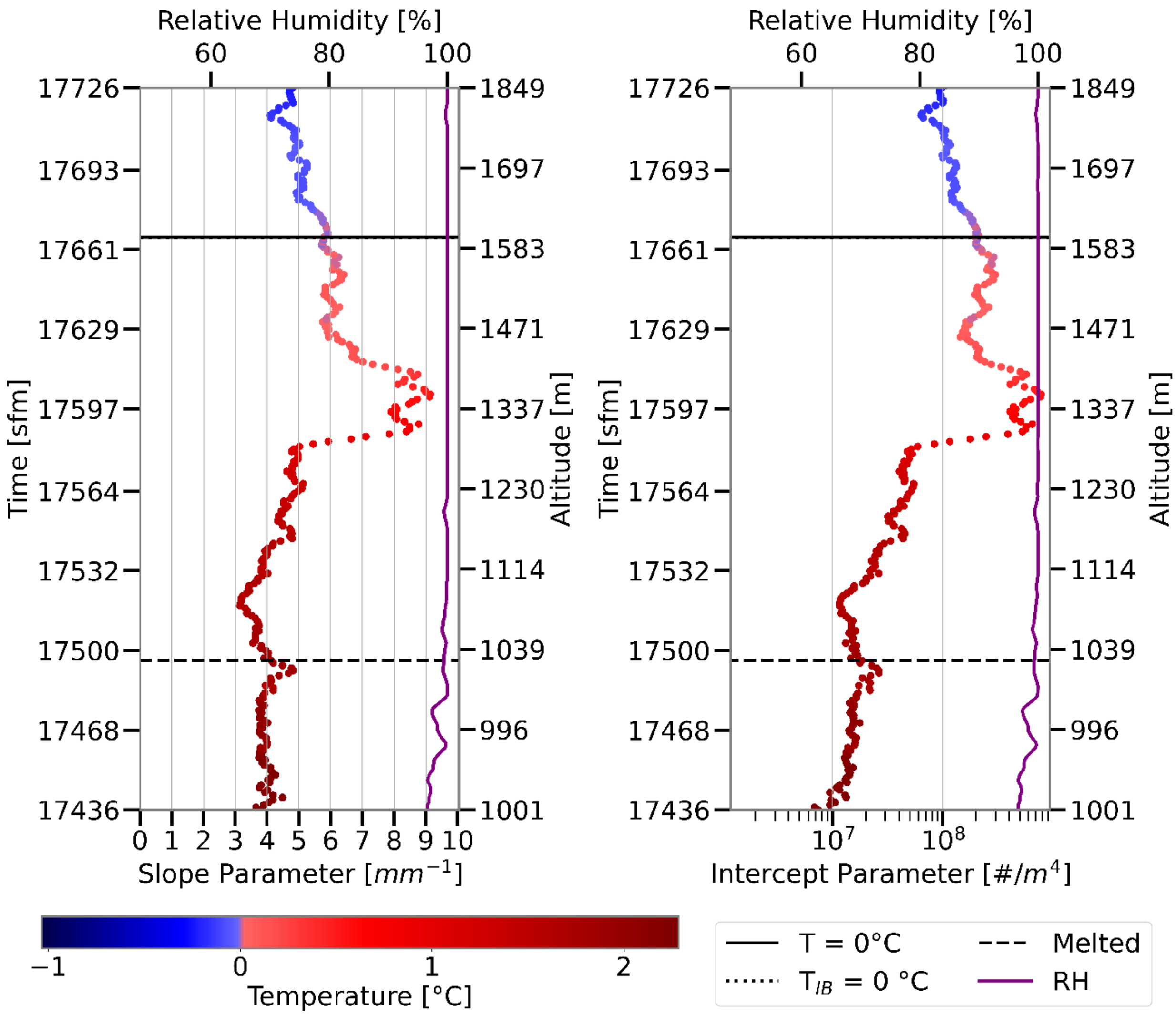

Figure 16: Plots similar to Figure 12, except for showing the melting layer for the GCPEX_Spi-Asc_100RH case (Table 5).

4.3 High Relative Humidity

The OLYMPEX_Ram-Des_98RHa case is representative of many of the melting layers with greater than 95 percent relative humidity. Over the melting layer depth of 261 m, maximum diameter steadily decreases while area ratio of large hydrometeors steadily increases (Figure 17). Above the melting layer, the area ratio values vary with hydrometeors size, with larger hydrometeors having lower area ratio. At the melting layer top, area ratio of hydrometeors less than 1,000 µm rapidly increases by 0.2. From the top to the bottom of the melting layer, maximum diameter decreases by approximately 13,000 µm, from 16,000 µm to 3,000 µm, suggesting there is no enhanced aggregation occurring in the melting layer. The area ratio of the large hydrometeors reaches a maximum of approximately 0.8 at the melting layer bottom, matching the raindrop value in Heymsfield et al. (2015). Within and below the melting layer depth, the concentration of hydrometeors smaller than 1,000 µm slightly increases.

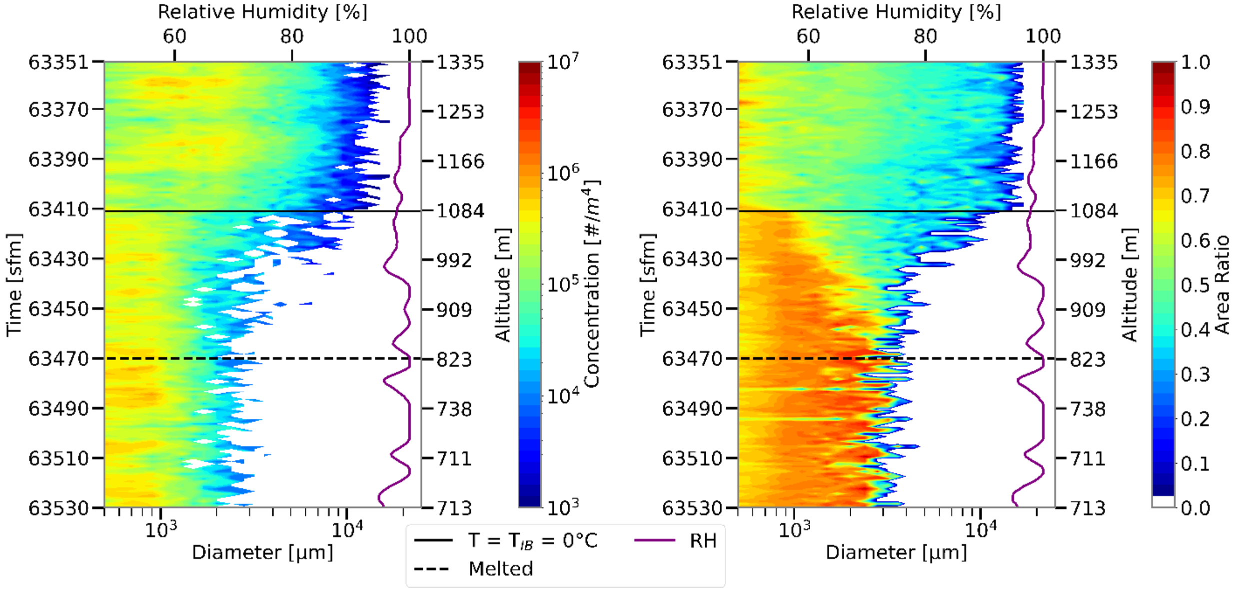

Figure 17: Plots similar to Figure 11, except for showing the melting layer for the the OLYMPEX_Ram-Des_98RHa case (Table 5).

Like the saturated cases, the change in the slope and shape parameter within the melting layer varies greatly between the cases with greater than 90 percent relative humidity. During OLYMPEX_Ram-Des_98RHa, both the slope and intercept parameter increase at the melting layer top (Figure 18), located with the decrease of maximum hydrometeor diameter and a slight increase in concentration of small hydrometeors (Figure 17). Broadly, the slope and intercept parameters increase from the melting layer top towards the bottom at a much lesser magnitude, similar to OLYMPEX_Ram_Des_100RH (Figure 12). Of the other thirteen cases between 95 percent and 100 percent relative humidity, both parameters overall increase through the melting layer in eight cases compared to both parameters decreasing in just one case. In the remaining four cases, the parameters vary.

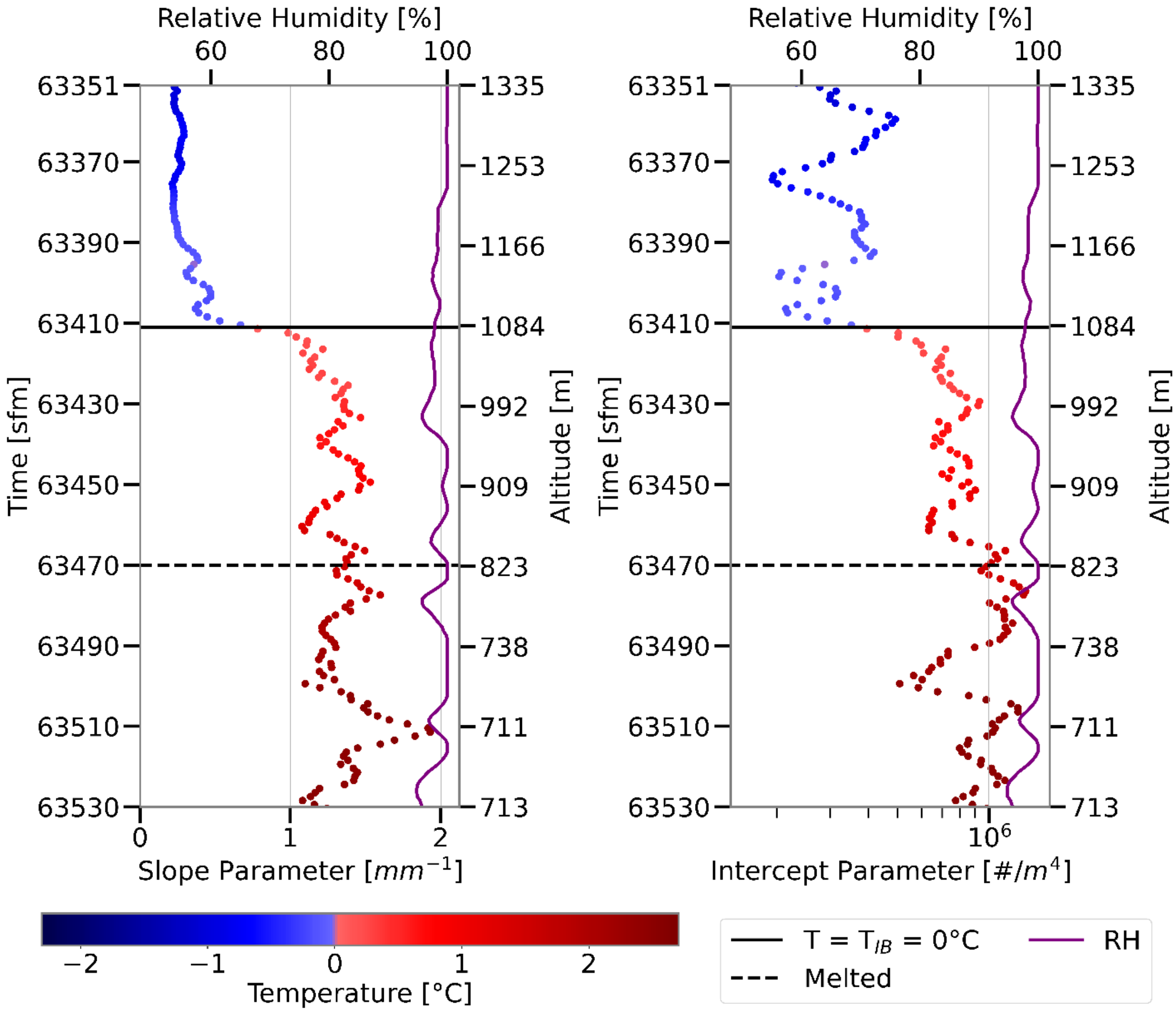

Figure 18: Plots similar to Figure 12, except for showing the melting layer for theOLYMPEX_Ram-Des_98RHa case (Table 5).

The IPHEX_Spi-Asc_100RH melting layer has lower total concentration than all of the other cases, especially for hydrometeors smaller than 1,000 µm (Figure 19). Additionally, the area ratio is generally higher than other cases. Nevertheless, area ratio noticeably increases towards the melting layer bottom for larger hydrometeors. Where concentration is low, approximately 10^5 #/m^4 and less, the area ratio is high, even for frozen hydrometeors. The larger than expected area ratio values suggests that high concentration values are important to accurately measure the area ratio of hydrometeors. Contrary to expectations, there are lower area ratio values below the melting layer, associated with a large increase in concentration of hydrometeors that are 700 µm and smaller. Despite low concentration values, there is a peak in maximum diameter in the middle of the melting layer suggesting aggregation may be occurring; however, there are two additional distinct peaks, one above the melting layer and one below. These peaks in maximum diameter may be a result of the aircraft encountering inhomogeneities in the cloud during its spiral, rather than a direct result of the melting layer.

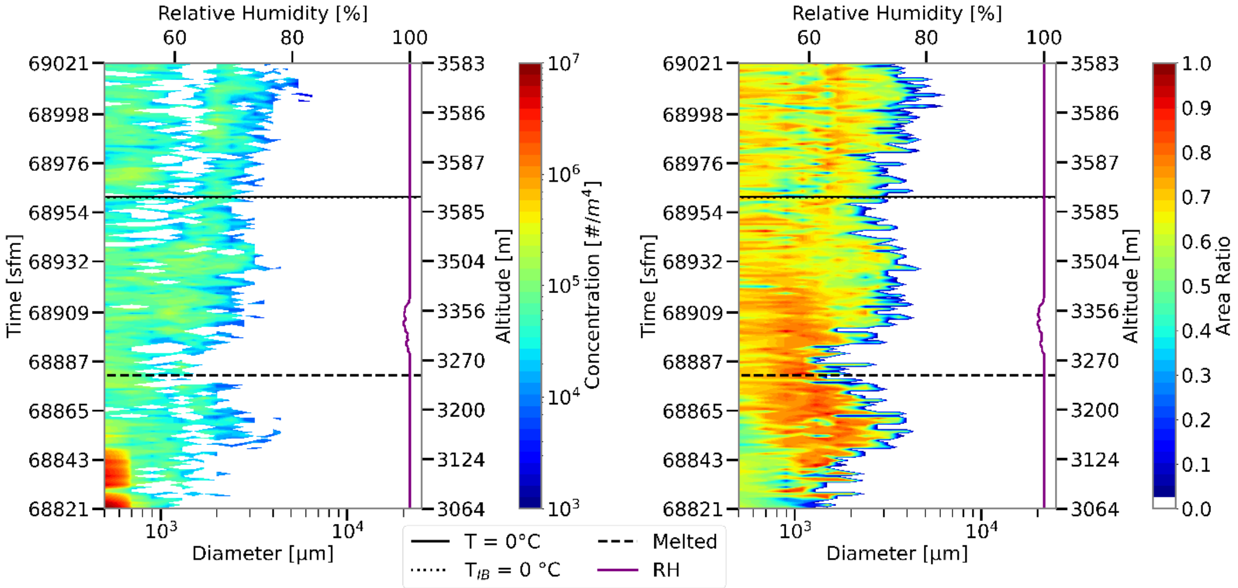

Figure 19: Plots similar to Figure 11, except for showing the melting layer for the IPHEX_Spi-Asc_100RH case (Table 5).

Two of the four melting layer cases with relative humidity between 90 and 95 percent (OLYMPEX_Ram-Des_91RH, OLYMPEX_Ram-Des_92RH) are similar to cases with higher relative humidity, while the remaining two (IPHEX_Ram-Asc_92RH, IMPACTS_Spi-Des_94RH) differ. During IPHEX_Ram-Asc_92RH, the aircraft exits the cloud just below the melting layer bottom. Although concentration is above the 10^3 #/m^4 concentration threshold for a cloud through the entire melting layer depth, the maximum diameter rapidly decreases towards the melting layer bottom despite no significant changes in relative humidity (Figure 20). Starting approximately 80 m below the melting layer bottom, no hydrometeors are detected in a roughly 200 m thick layer. Still, the IPHEX_Ram-Asc_92RH melting layer presents an increase in area ratio for hydrometeors about 1,000 µm and smaller.

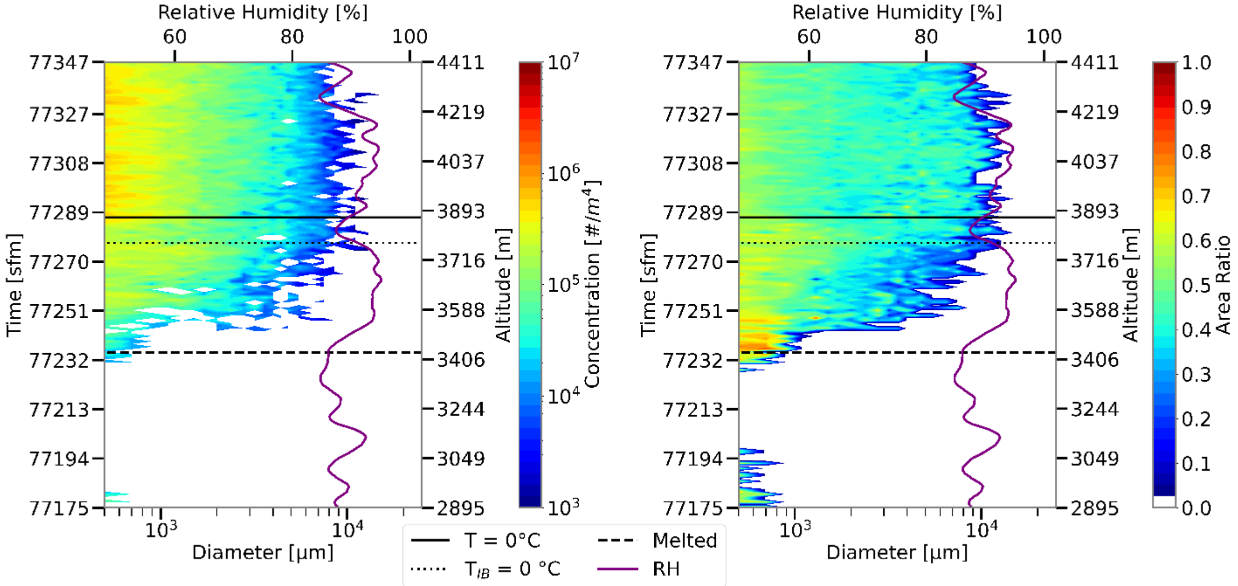

Figure 20: Plots similar to Figure 11, except for showing the melting layer for the IPHEX_Ram-Asc_92RH case (Table 5).

Even though the relative humidity is 93.7 percent, IMPACTS_Spi-Des_94RH has the most significantly increased aggregation in the melting layer. From above the melting layer to the top, maximum diameter is approximately 3,000 µm (Figure 21). The maximum diameter increases until approximately 250 m below the melting layer top, where it peaks at 18,000 µm in an approximately150 m thick layer. In the 100 m thick layer towards the melting layer bottom, maximum diameter decreases back to 3,000 µm. The area ratio of the largest hydrometeors above the aggregation layer is approximately 0.1-0.2. In the aggregation layer, area ratio of the largest hydrometeors is approximately 0.3-0.5. There is an initial increase in area ratio of the smallest hydrometeors with 500 µm diameter by 0.1 just below the melting layer top. By 200 m below the melting layer top, area ratio increases from the smallest to largest hydrometeors, in the middle of the aggregation layer. As maximum diameter decreases, area ratio increases until the melting layer bottom where hydrometeors have an area ratio of approximately 0.6-0.7.

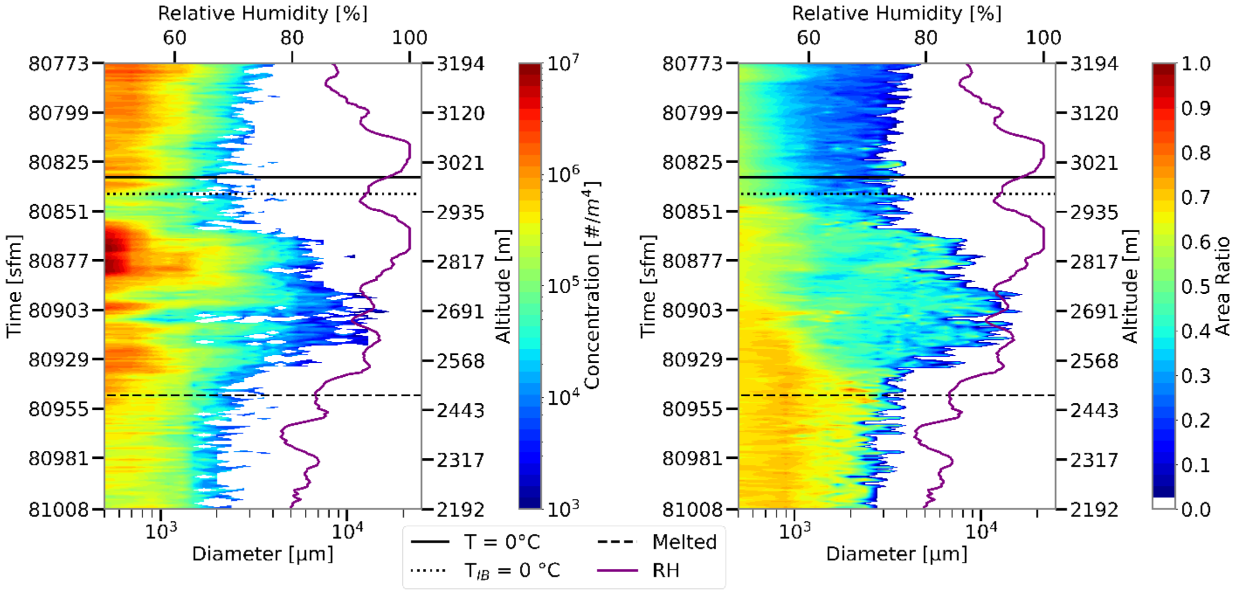

Figure 21: Plots similar to Figure 11, except for showing the melting layer for the IMPACTS_Spi-Des_94RH case (Table 5).

From the exponentially fitted size distribution for IM1, the slope parameter is fairly consistent throughout besides two large spikes (Figure 22). Above the melting layer, the slope parameter increases by approximately 0.5 mm^{-1}, while the intercept parameter does not change much. Both parameters experience a significant spike approximately 150 m below the melting layer top (Figure 22), associated with an increased concentration of small hydrometeors (Figure 21). From approximately 50 m above the melting layer bottom to below the melting layer, the intercept parameter decreases by approximately an order of magnitude, while the slope parameter decreases by approximately 1 mm^{-1} (Figure 22). For a brief period below the first spike, both parameters experience a local minimum (Figure 22) where the concentration of small hydrometeors returns to similar values at the melting layer top and above (Figure 21). The larger hydrometeors likely cause the exponential fit to produce smaller intercept and slope values than the melting layer top and above.

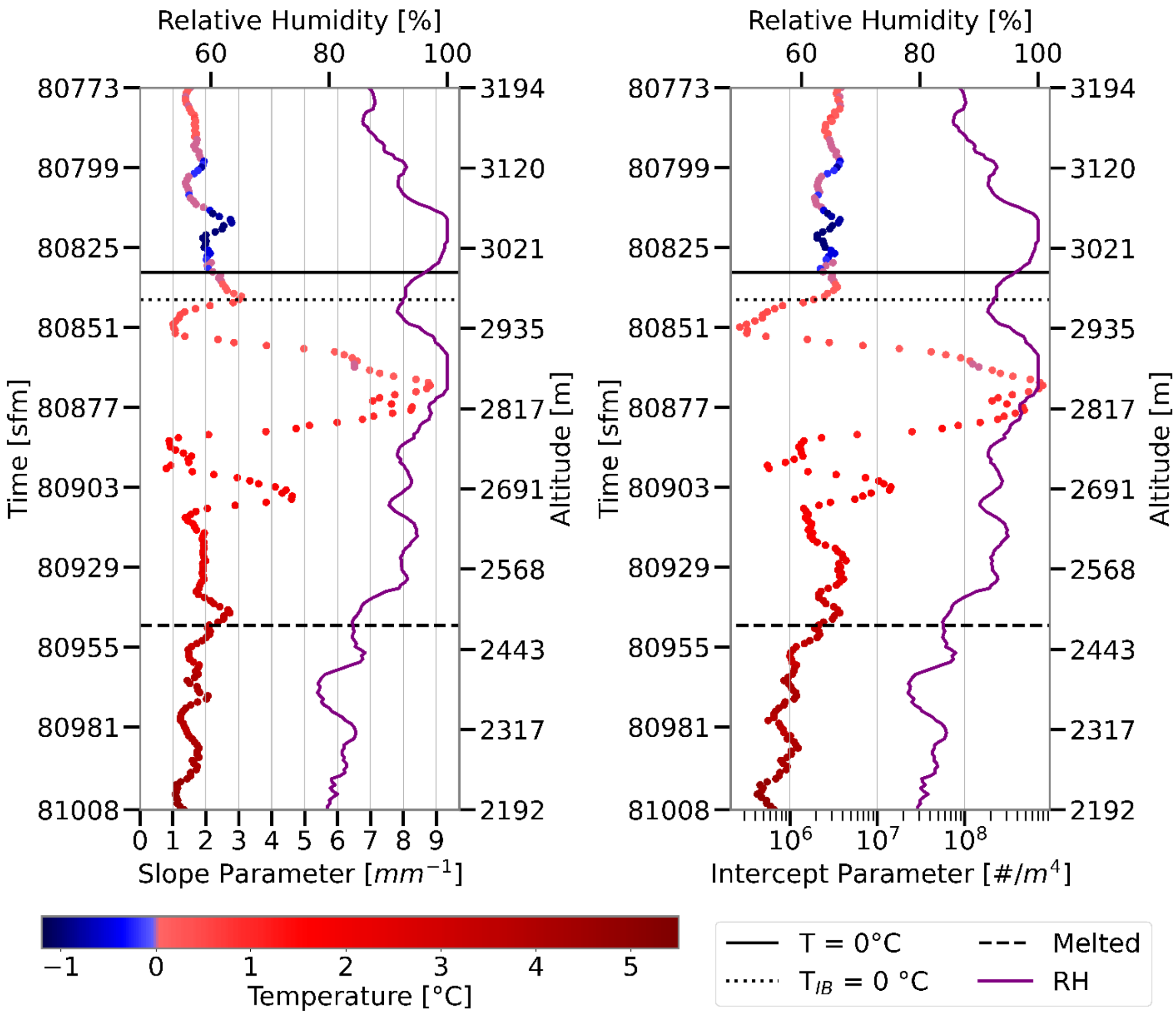

Figure 22: Plots similar to Figure 12, except for showing the melting layer for the IMPACTS_Spi-Des_94RH case (Table 5).

Two of the high relative humidity melting layers exhibit a nearby 0 °C quasi-isothermal layer. During IMPACTS_Ram-Asc_95RH, there is an approximately 400 m deep layer of near 0 °C air temperature (Figure 23). In the isothermal layer, hydrometeors are not melting yet because the ice-bulb temperature is still below 0 °C. The ice-bulb temperature slowly increases throughout the isothermal layer as relative humidity increases but does not reach 0 °C until just below the isothermal layer. Thus, unlike previous studies (e.g., Wexler et al. 1954; Atlas et al. 1969; Carbone 1982; Stewart et al. 1984; Szeto and Stewart 1997; Kain et al. 2000) melting is not responsible for this isothermal layer. Once melting begins, temperature increases to above 1 °C before briefly spiking to around 0.5 °C then increasing above 1 °C again. During GCPEX_Spi-Asc_100RH, the second 0 °C quasi-isothermal layer is recorded (Figure 24). The lapse rate starts to decrease above the melting layer and continues into the melting layer producing an approximately 350 m quasi-isothermal layer where temperatures range from -0.1 °C to 0.2 °C. The depth of the isothermal layer is about evenly split between a section above and below melting layer top. The onset of melting appears to have no impact on the isothermal layer. Contrasting IMPACTS_Ram-Asc_95RH, the isothermal layer is fully saturated throughout. The IMPACTS_Ram-Asc_95RH and GCPEX_Spi-Asc_100RH cases are the only two in the entire dataset that experience a quasi-isothermal layer.

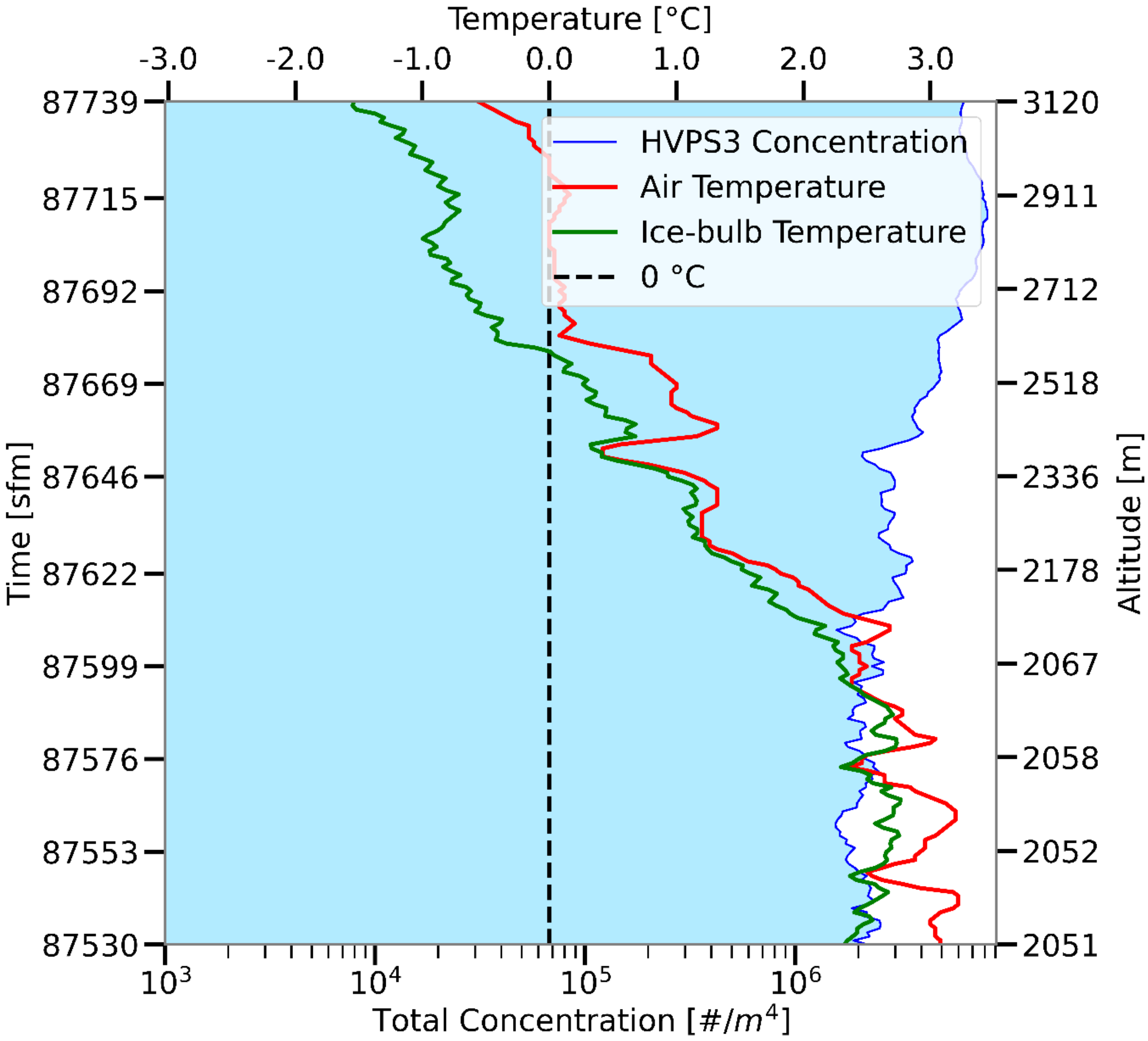

Figure 23: Plots similar to Figure 5, except for showing the melting layer for the IMPACTS_Ram-Asc_95RH case (Table 5).

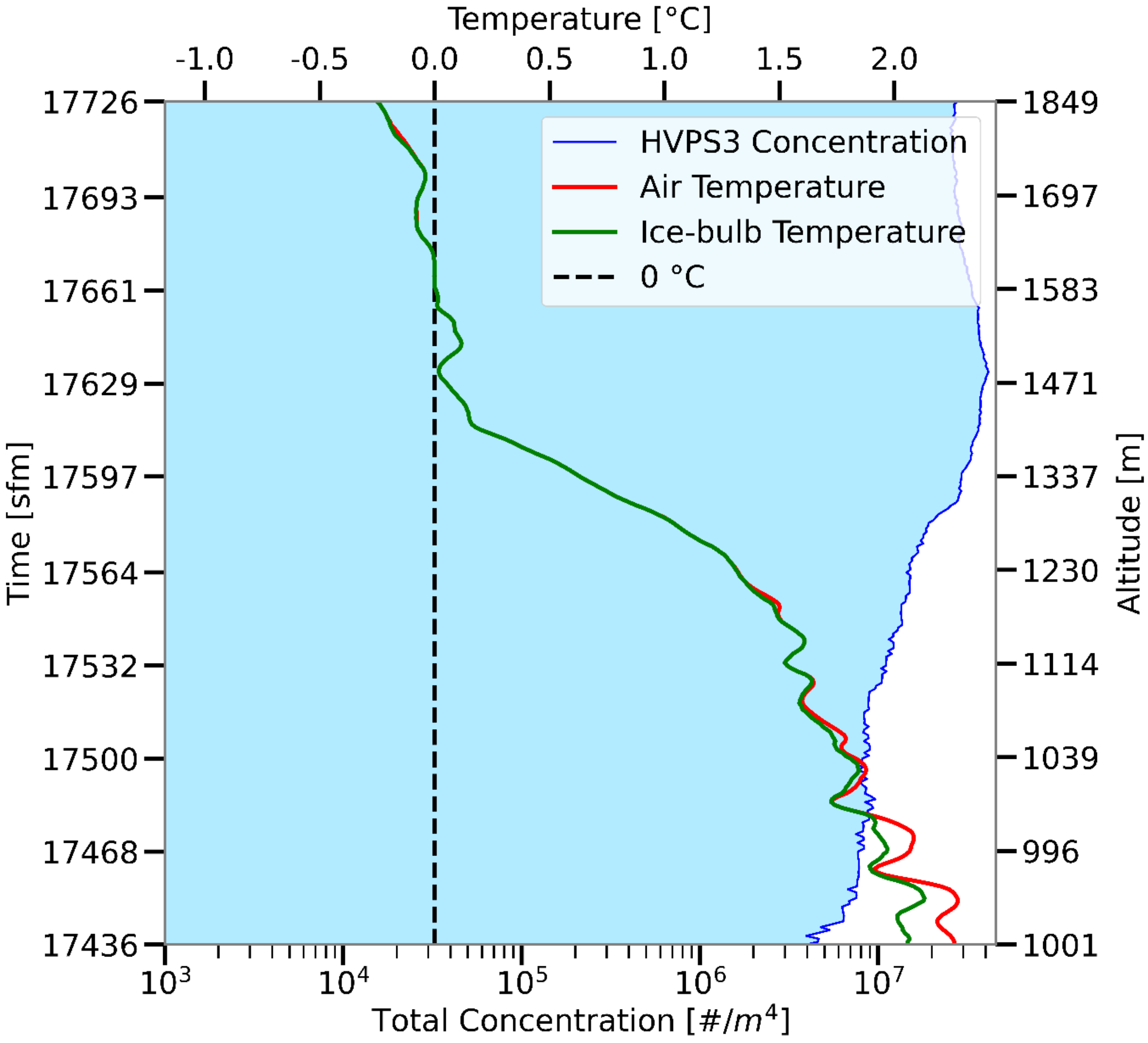

Figure 24: Plots similar to Figure 5, except for showing the melting layer for the GCPEX_Spi-Asc_100RH case (Table 5).

4.4 Low Relative Humidity Cases

The nine low relative humidity cases have the greatest variation between each other. During MC3E_Ram-Asc_83RHa, there is a local minimum in relative humidity between the 0 °C air temperature isotherm and the melting layer top at the 0 °C ice-bulb isotherm (Figure 25). Below the relative humidity minimum, there is a peak in both maximum diameter at 18,000 µm and relative humidity at approximately 90 percent in a 200 m thick layer near the melting layer top. Notably, the area ratio of small hydrometeors does not increase until the ice-bulb temperature exceeds 0 °C. Similar to IMPACTS_Spi-Des_94RH where significantly enhanced aggregation also occurred (Figure 21), area ratio starts to increase as maximum diameter decreases (Figure 25). During MC4, the slope and intercept parameter experience a local minimum in the location of aggregation and large maximum diameters, which is also similar to IMPACTS_Spi-Des_94RH (Figure 26). The GCPEX_Spi-Des_84RH melting layer differs from MC3E_Ram-Asc_83RHa and is more similar to the high relative humidity cases. The maximum diameter does not increase around the melting layer top, suggesting that aggregation is not occurring at a similar magnitude (Figure 27). However, the maximum diameter above the melting layer is larger in GCPEX_Spi-Des_84RH than MC3E_Ram-Asc_83RHa at approximately 8,000 µm compared to 3,000 µm, respectively. Otherwise, during GCPEX_Spi-Des_84RH, area ratio increases from small to large hydrometeors.

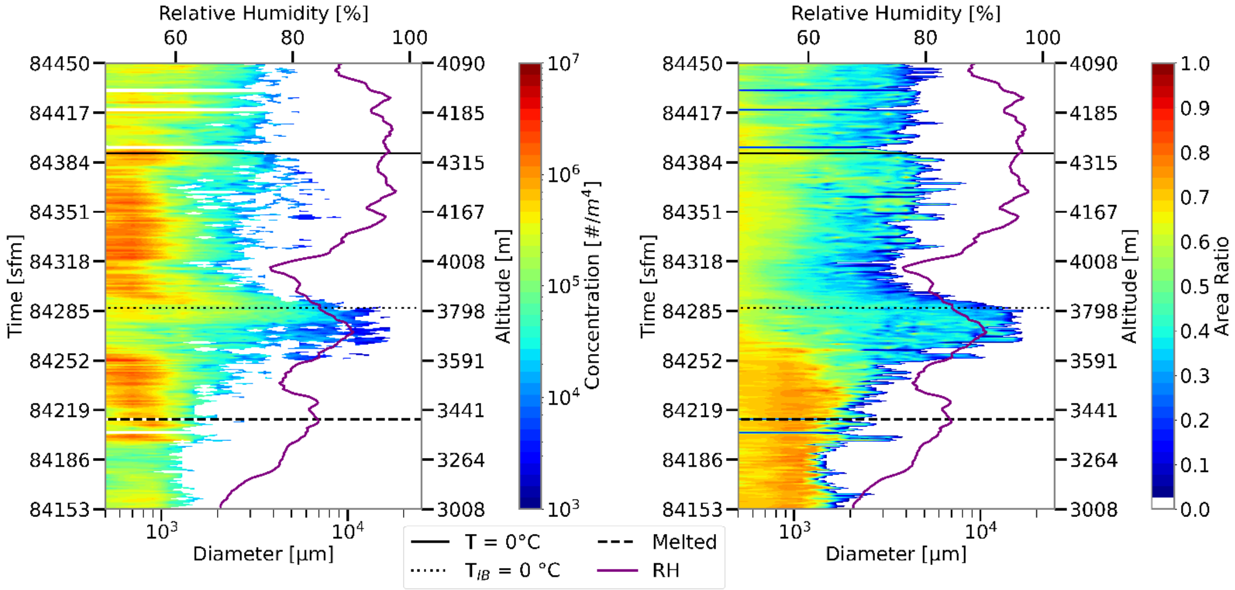

Figure 25: Plots similar to Figure 12, except for showing the melting layer for the MC3E_Ram-Asc_83RHa case (Table 5).

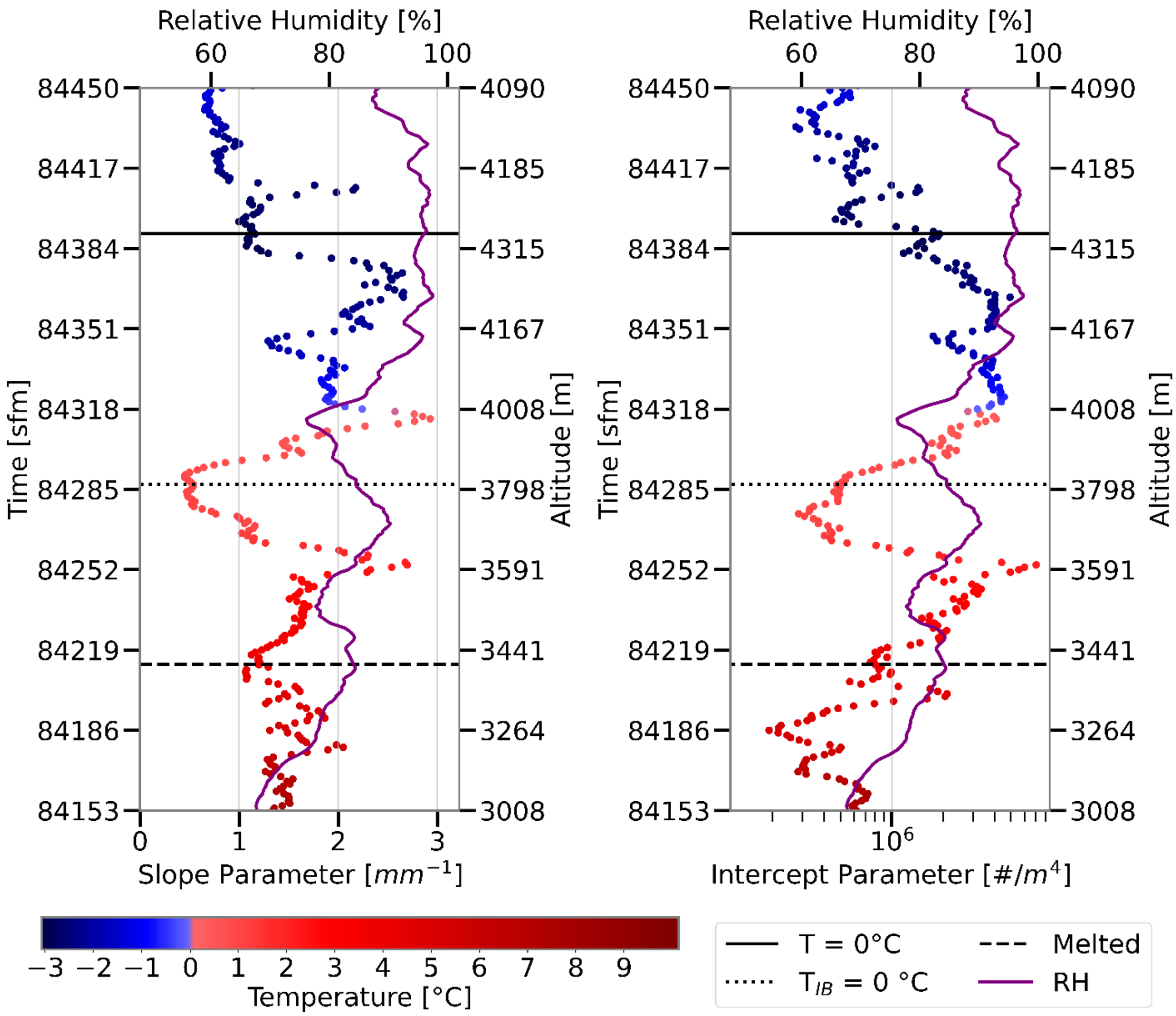

Figure 26: Plots similar to Figure 12, except for showing the melting layer for the MC3E_Ram-Asc_83RHa case (Table 5).

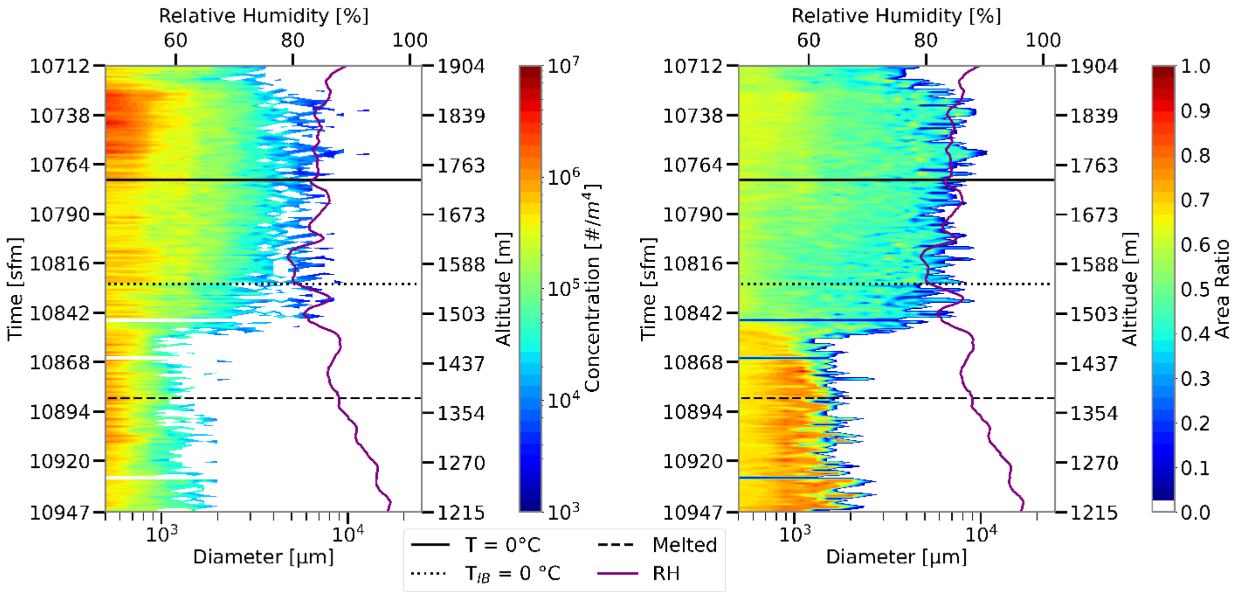

Figure 27: Plots similar to Figure 11, except for showing the melting layer for the GCPEX_Spi-Des_84RH case (Table 5).

Two melting layer profiles are recorded consecutively on 10 MAY 11 (MC3E_Ram-Des_79RH and MC3E_Ram-Asc_83RHb) during a ramp descent followed by a ramp ascent (Figure 28). In total, there are approximately 3 s of below melting layer observations; however, the melting layer was still fully sampled during both cases. During the MC3E_Ram-Asc_83RHb ascent, the 0 °C isotherm is 235 m higher than it was during the MC3E_Ram-Des_79RH descent. Despite the air temperature difference, the 0 °C ice-bulb isotherm is roughly the same altitude at approximately 3,750 m due to lower relative humidity conditions above the melting layer during the MC3E_Ram-Asc_83RHb ascent. Thus, both melting layers have similar depths of 133 m for MC3E_Ram-Des_79RH and 123 m for MC3E_Ram-Asc_83RHb. During the MC3E_Ram-Des_79RH descent, area ratio values are relatively high at 0.4-0.7 in and above the melting layer (Figure 29). At the bottom of the 123 m deep melting layer, the area ratio of the largest remaining hydrometeors increases to above 0.7. Also at the melting layer bottom, maximum diameter rapidly decreases. During the MC3E_Ram-Asc_83RHb ascent, maximum diameter slowly increases going up the melting layer depth while area ratio decreases (Figure 30). Compared to the

MC3E_Ram-Des_79RH descent (Figure 29), the MC3E_Ram-Asc_83RHb ascent contains approximately 5,000-7,000 µm larger maximum hydrometeor diameter and 0.2 lower area ratio values at the melting layer top and above (Figure 30). During MC3E_Ram-Asc_83RHb, the area ratio of hydrometeors also slowly increases from the melting layer top to the bottom, starting with small hydrometeors. The differences between these two back-to-back cases suggest there are inhomogeneities in the clouds between the two ramps as the aircraft traveled approximately 13 km horizontally (Figure 28). The inhomogeneities may be due to entrainment in the deep convective storms focused on during MC3E (e.g., Freud et al. 2011; Guo et al. 2015), which would also explain the relative humidity differences.

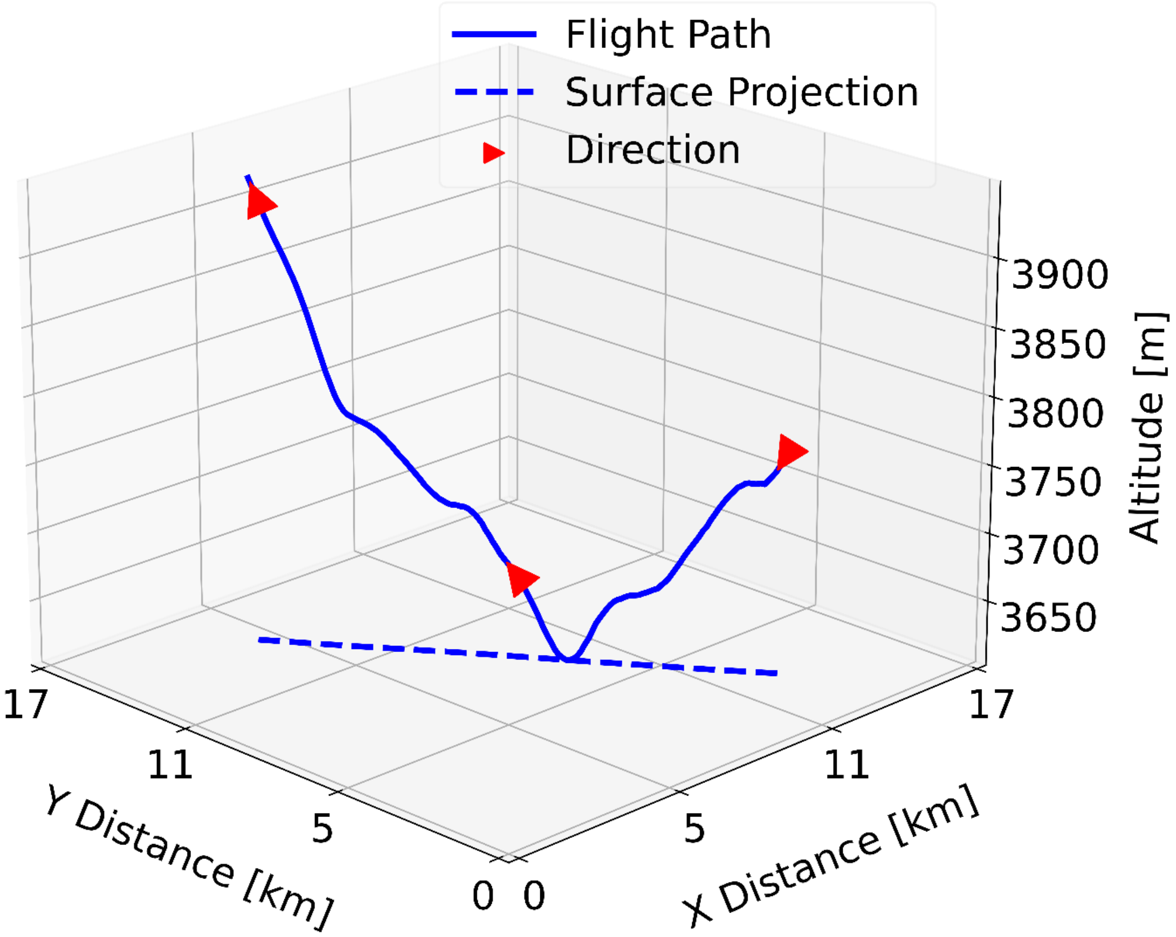

Figure 28: Plot showing the flight path (solid blue line) and the surface projection (dashed blue line) of the aircraft sampling two melting layers consecutively (MC3E_Ram-Des_79RH and MC3E_Ram-Asc_83RHb) on 11 MAY 2010 during MC3E (Table 5). The flight path starts at the

0 °C isotherm encountered during the MC3E_Ram-Des_79RH descent and ends at the 0 °C isotherm encountered during the MC3E_Ram-Asc_83RHb ascent. The red arrowhead indicates the direction of the aircraft. The X Distance shown is latitudinal distance while the Y Distance is longitudinal distance.

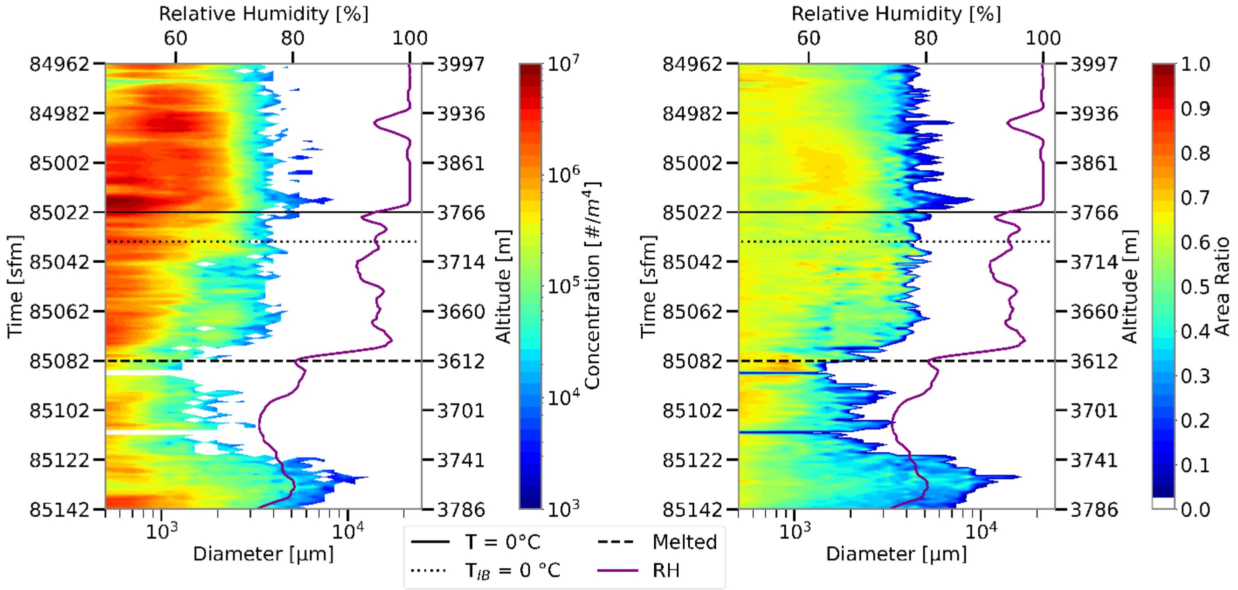

Figure 29: Plots similar to Figure 11, except for showing the melting layer for the MC3E_Ram-Des_79RH case (Table 5).

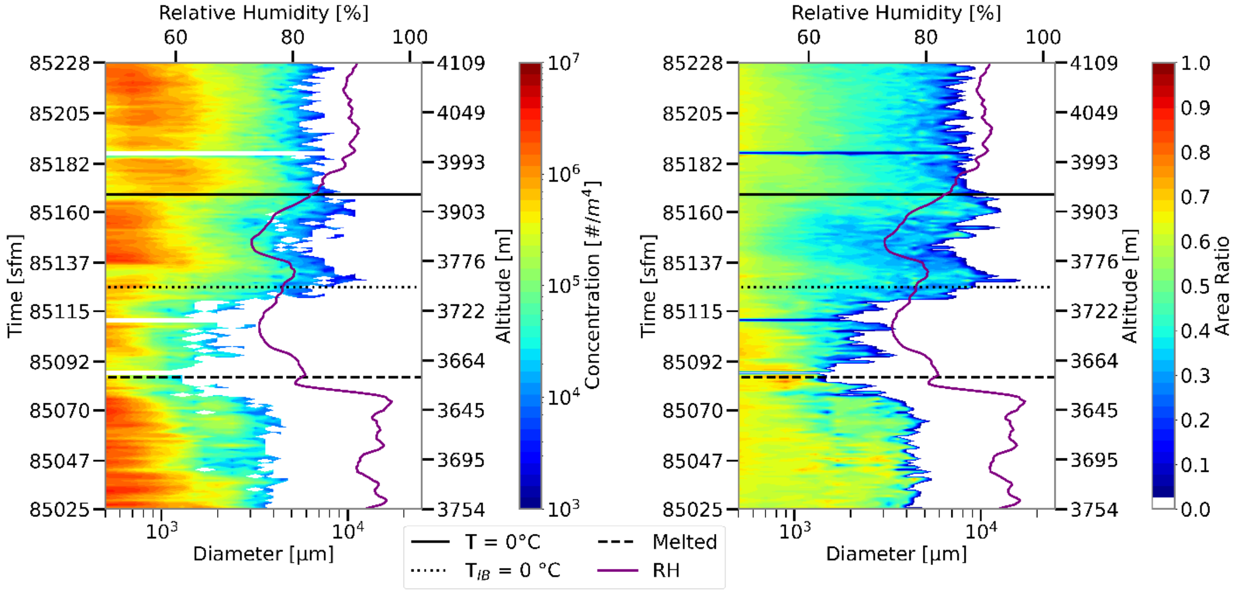

Figure 30: Plots similar to Figure 11, except for showing the melting layer for the MC3E_Ram-Asc_83RHb case (Table 5).

Three melting layers are sampled below 75 percent relative humidity. During MC3E_Spi-Des_75RH, area ratio evolves similarly to other cases where it does not begin to increase until below the 0 °C ice-bulb isotherm (Figure 31). Hydrometeor concentration decreases with decreasing altitude, likely due to the greatly subsaturated conditions as relative humidity also decreases with decreasing altitude. During GCPEX_Ram-Des_71RH, maximum diameter is decreasing above the melting layer top (Figure 32). In the top 150 m of the melting layer, maximum diameter increases to approximately 6,000 μm, likely due to enhanced aggregation, even with relative humidity around 70 percent. In the lower 150 m of the melting layer, maximum diameter decreases as area ratio increases; however, the HVPS3 measures zero counts, suggesting that the aircraft goes in and out of clouds.

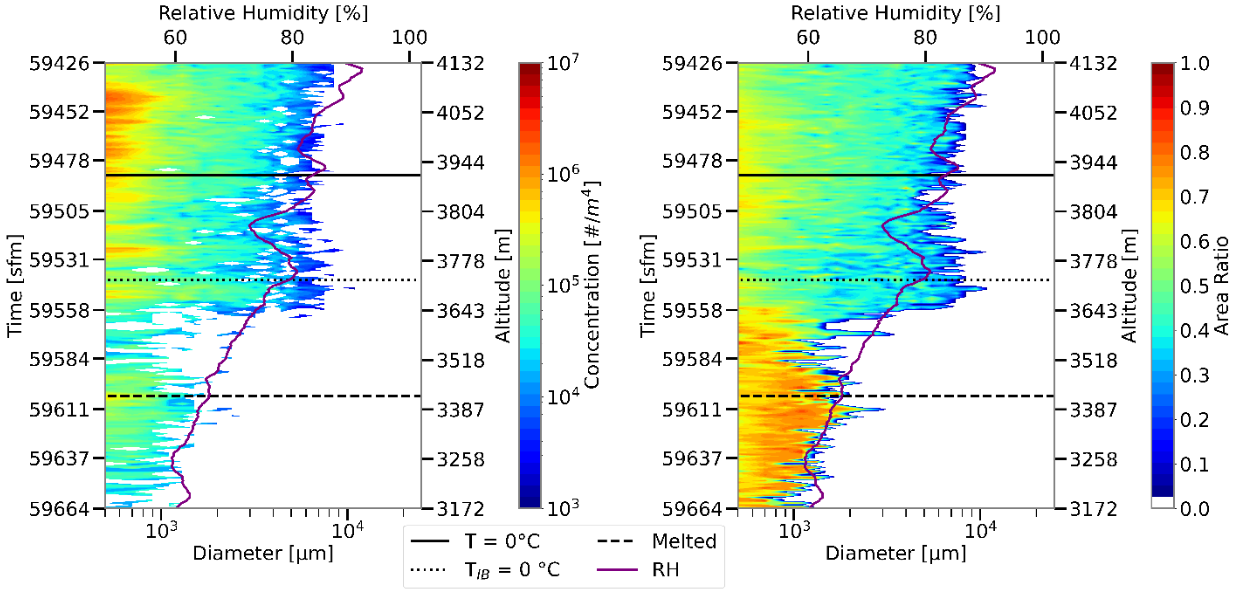

Figure 31: Plots similar to Figure 11, except for showing the melting layer for the MC3E_Spi-Des_75RH case (Table 5).

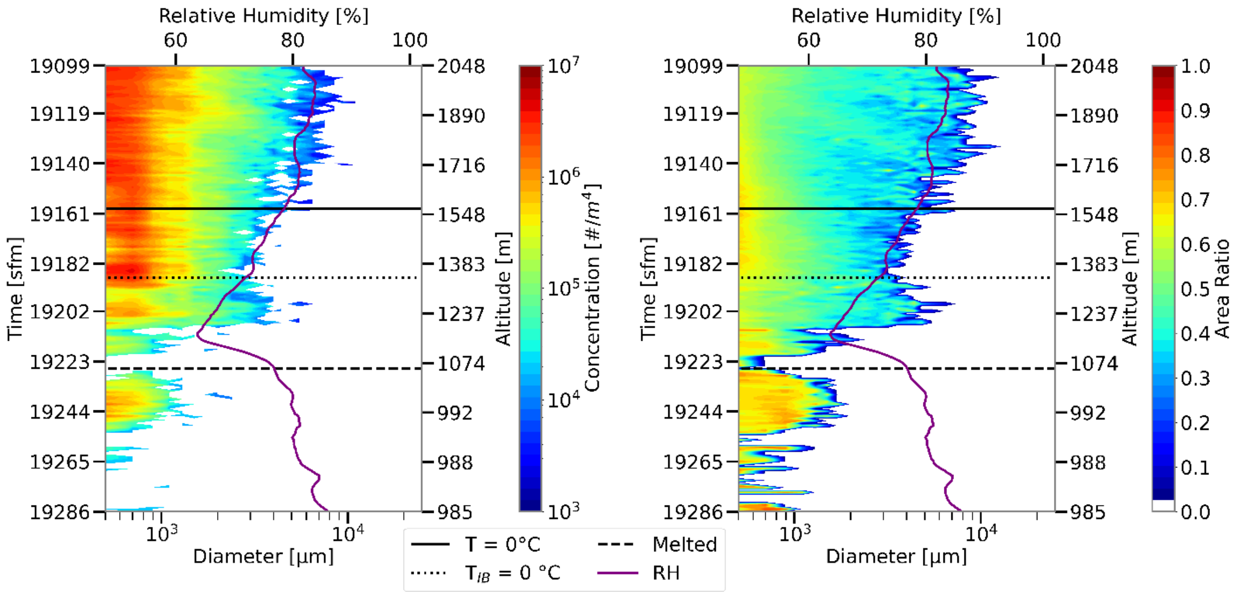

Figure 32: Plots similar to Figure 11, except for showing the melting layer for the GCPEX_Ram-Des_71RH case (Table 5).

The lowest relative humidity case is MC3E_Spi-Des_63RH. Despite the 63 percent relative humidity, total hydrometeor concentration remained high (Figure 33). However, the concentration of hydrometeors between 800 μm and 1,110 μm slowly decreases until the melting layer top (Figure 33). In a depth of approximately 100 m below the melting layer top, maximum diameter increases from approximately 11,000 μm to 14,000 μm, suggesting that aggregation is still occurring even in relative humidity conditions of approximately 75 percent. Below the melting layer top, maximum diameter and concentration slowly decreases. Area ratio increases from the smallest to largest hydrometeors from 0.3-0.6 to 0.7-0.9. From the exponential fit, the intercept parameter decreases from above the melting layer to the top, while the slope parameter slightly increases from 0 °C air temperature to the melting layer top (Figure 34). In the melting layer, the parameters vary, likely due to zero hydrometeor counts resulting in less consistent concentration measurements from the HVPS3 (Figure 33). However, the intercept parameters trend downward through the melting layer, and the slope parameter first trends upward until about the middle of the melting layer before decreasing to a local minimum when all hydrometeors are melted (FIG).

Below the melting layer, the intercept parameter starts to increase, collocated with an increase in concentration of hydrometeors smaller than 10^3 µm (Figure 34; Figure 33). The slope parameter does not change much below the melting layer due to the increases in intercept parameter, maximum diameter, and hydrometeor concentration of hydrometeors larger than 10^3 µm (Figure 34; Figure 33).

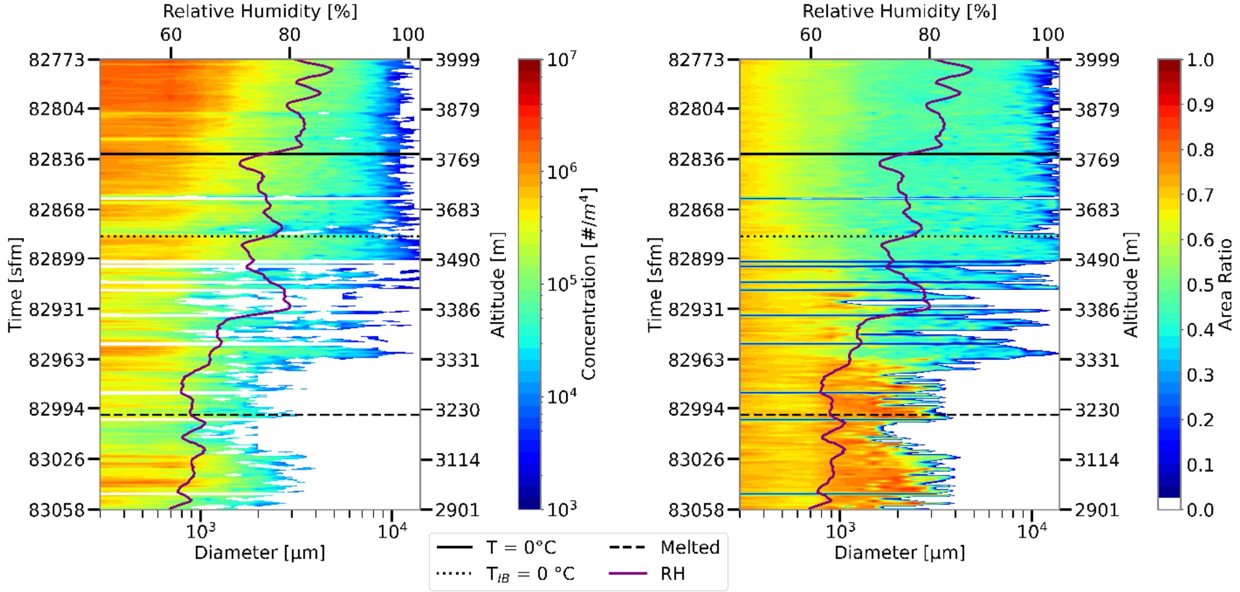

Figure 33: Plots similar to Figure 11, except for showing the melting layer for the MC3E_Spi-Des_63RH case (Table 5).

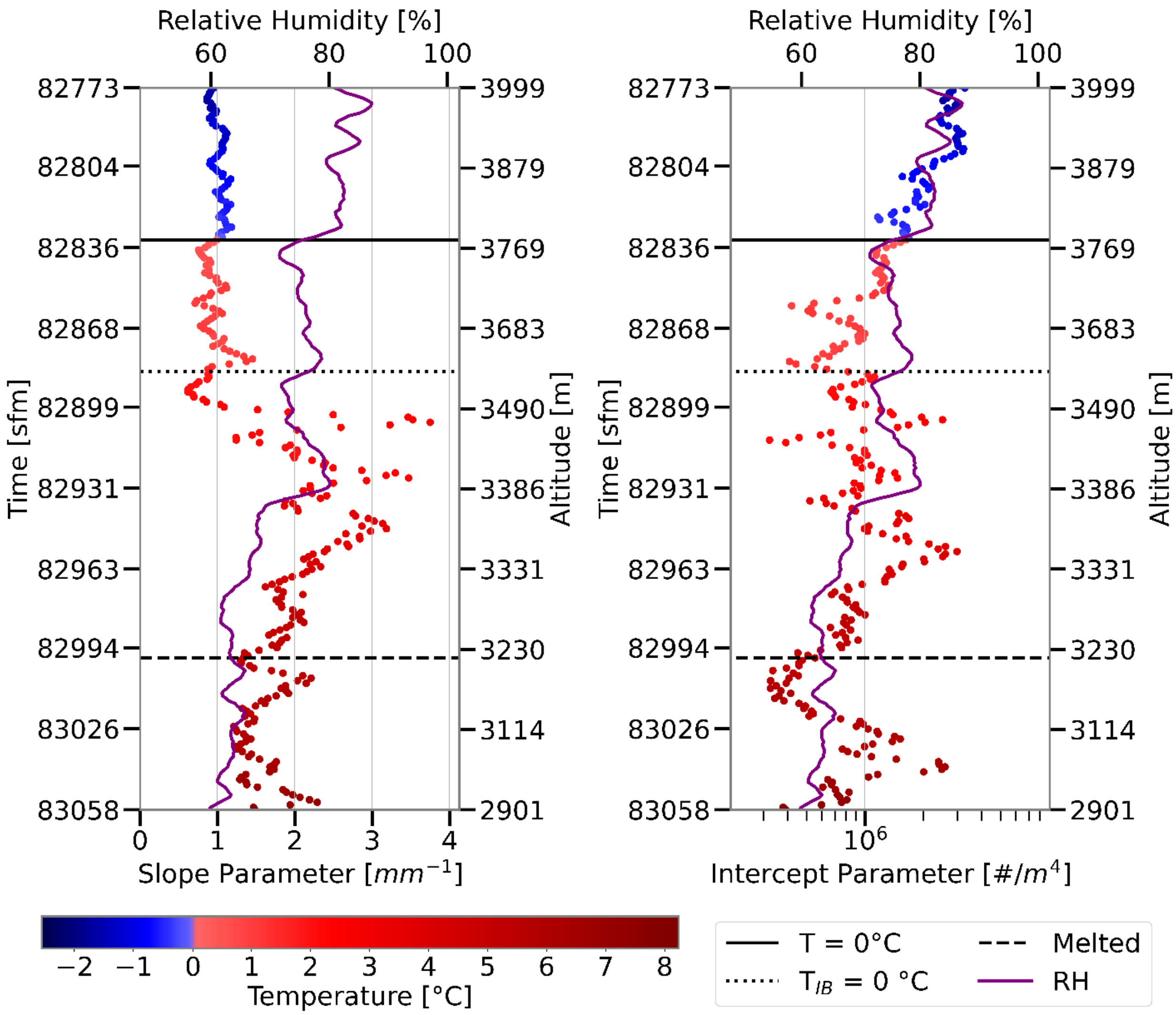

Figure 34: Plots similar to Figure 12, except for showing the melting layer for the MC3E_Spi-Des_63RH case (Table 5).

CHAPTER 5

SUMMARY AND DISCUSSION

A total of thirty-three melting layers profiled during five recent NASA field campaigns are analyzed. The field campaigns focused on a variety of cloud types and storm environments, as well as varying locations and seasons (Table 6). During MC3E and IPHEX, deep convective storms were sampled during the springtime in the United States. The focus of MC3E was on the Great Plains while IPHEX focused on the southeastern US. Both GCPEX and IMPACTS sampled storms during wintertime; however, the focus of GCPEX was on lake effect precipitation in southeastern Ontario, Canada and the focus of IMPACTS was on snow bands in the northeast US. In the stratiform clouds sampled during GCPEX, the maximum diameter of hydrometeors is generally smaller than other field projects. During IMPACTS, typically snow bands were crossed horizontally, thus there are few vertical profiles of the melting layer. Additionally, the winter conditions during GCPEX and IMPACTS resulted in temperatures that were typically too cool for a melting layer to be sampled. Most of the melting layer cases are from OLYMPEX, which focused on precipitation around Mount Olympus located in northwestern Washington, US. OLYMPEX was conducted during late fall to assess how well satellites accurately measure both rainfall and snowfall; thus, conditions were often favorable for mixed-phase precipitation and vertical profiles of the melting layer.

Table 6: Table summarizing the cloud types and locations of recent NASA field projects analyzed for hydrometeor changes within the melting layer. Field project acronyms used are Mid-latitude Continental Convective Clouds Experiment (MC3E); Global Precipitation Measurement (GPM) Cold-season Precipitation Experiment (GCPEX); Integrated Precipitation and Hydrology Experiment (IPHEX); Olympic Mountain Experiment (OLYMPEX); Investigation of Microphysics and Precipitation for Atlantic Coast-Threatening Snowstorms (IMPACTS).

Project	Season	Cloud Type	Location
MC3E	Spring	Deep Convective Clouds	Oklahoma, US
GCPEX	Winter	Stratiform Precipitation, Lake Effect	Georgian Bay, Canada
IPHEX	Spring	Deep Convective Clouds	Southeast US

OLYMPEX	Fall	Deep Cloud Layers	Washington State, US
IMPACTS	Winter	Snow Bands	Northeast US

Table 7: Table summarizing the changes in hydrometeor concentration (conc), area ratio, maximum diameter (max D), and the slope (λ) and intercept parameter (N_0) from the exponential fit to the size distribution throughout the melting layer. Small hydrometeors are 1,000 µm and less, whereas large hydrometeors have a greater diameter. The first (blue) indicators are for the transition from above to inside the melting layer. The second (red) indicators are for the transition from the melting layer to below. An up arrow is an increase, a down arrow is a decrease, an equal sign is no change, and a dash is no measurements. Having the first and second indicators the same denotes no change throughout the entire melting layer depth (i.e., no steady state is reached and no transition occurs). Case groups are alternatively shaded based on the relative humidity range.

Case	**Conc**				**Area Ratio**				**Max D**		**Fit**			
	Small		Large		Small		Large		All		N_0		λ	
OLYMPEX_Spi-Des_100RHa	↑	↓	=	=	↓	=	↑	↑	↓	=	↑	↓	↑	↓
OLYMPEX_Ram-Des_100RH	↑	=	↓	↓	↑	=	↑	=	↓	=	↑	↑	↑	↑
OLYMPEX_Spi-Des_100RHb	↑	↓	↓	=	↑	=	↑	=	↓	↑	↑	↑	↑	↑
OLYMPEX_Spi-Des_100RHc	↓	=	=	=	↑	=	↑	=	↓	=	↓	=	↓	=
GCPEX_Spi-Asc_100RH	↓	=	=	=	↑	=	↑	=	↓	↓	↑	↓	↑	↓
IPHEX_Spi-Asc_100RH	=	↑	=	=	↑	↓	↑	↑	=	=	↑	↑	↑	↑
GCPEX_Spi-Asc_99RH	=	=	=	=	↑	↑	=	↑	=	=	↓	↓	↑	↑
OLYMPEX_Spi-Asc_99RHa	↓	=	↓	↑	↑	=	↑	=	=	↓	↑	↑	↑	=
OLYMPEX_Ram-Des_99RH	↓	=	↓	=	↑	=	↑	=	↓	↓	↑	=	↑	↑
OLYMPEX_Spi-Asc_99RHb	=	=	↓	=	↑	=	↑	=	↓	=	=	=	↑	=
MC3E_Spi-Asc_99RH	↓	=	↓	=	↑	=	↑	=	↑	↓	↓	↑	=	↑
OLYMPEX_Ram-Des_98RHa	↑	↑	↓	=	↑	=	↑	=	↓	↓	↑	↑	↑	↑
OLYMPEX_Spi-Asc_98RH	=	=	↓	=	↑	=	↑	=	↓	↓	↑	=	↑	=
OLYMPEX_Ram-Des_98RHb	↓	=	↓	↓	↑	=	↑	↑	=	↓	↓	↓	↑	↓
GCPEX_Spi-Asc_97RH	↓	=	=	=	↑	=	↑	=	=	=	↑	↑	↑	↑
OLYMPEX_Ram-Des_96RH	=	=	↓	=	↑	=	↑	=	↓	↑	↑	=	↑	=
IMPACTS_Ram-Asc_95RH	↓	=	↓	=	↑	=	↑	=	↑	↓	↓	↑	↑	↑
OLYMPEX_Ram-Asc_95RH	=	=	=	=	↑	=	↑	↑	↓	↓	↑	=	↑	↓
MC3E_Spi-Des_95RH	=	=	=	=	↑	=	↑	=	↑	↓	↑	↑	↑	↑
MC3E_Spi-Des_95RH	↓	=	↓	=	↑	=	=	↑	↑	↓	↑	↓	↑	↓
IMPACTS_Spi-Des_94RH	↑	↓	↑	↓	↑	=	↑	=	↑	↓	=	↓	↑	↓
IPHEX_Ram-Asc_92RH	↓	-	=	-	↑	-	=	-	↓	↓	-	-	-	-
OLYMPEX_Ram-Asc_92RH	↓	=	=	-	↑	=	=	-	↓	=	↓	=	↑	=
OLYMPEX_Ram-Des_91RH	↓	↑	=	=	↑	=	↑	=	↓	=	↑	=	↑	=
MC3E_Spi-Asc_90RH	↓	=	↓	=	↑	=	↑	=	↓	↓	↓	=	↑	=
GCPEX_Spi-Des_84RH	↓	=	=	=	↑	=	↑	=	↓	=	↑	↓	↑	↓
MC3E_Ram-Asc_83RHa	=	↓	=	=	↑	=	↑	=	↑	↓	=	↓	=	↓
MC3E_Ram-Asc_83RHb	↓	-	↓	-	↑	-	↑	-	↓	-	↑	↑	↑	=
OLYMPEX_Ram-Asc_82RH	↓	=	-	-	↑	=	-	-	↓	=	-	-	-	-
MC3E_Ram-Des_79RH	↓	-	↓	-	↑	-	=	-	↓	-	=	↓	↑	↓
MC3E_Spi-Des_75RH	↓	=	↓	-	↑	=	↑	-	↓	=	↓	↑	↑	↓

GCPEX_Ram-Des_71RH	↓	↓	=	↓	↑	↑	=	↑	↑	↓	-	-	-	-
MC3E_Spi-Des_63RH	↓	=	↓	=	↑	=	↑	=	↑	↓	=	↓	↑	↓

The most common trend overall is an increase in the small hydrometeor area ratio during the transition from above to within the melting layer (Table 7). In the single case (OLYMPEX_Spi-Des_100RHa) where the area ratio of small hydrometeors decreases, the area ratio measurements are generally lower than other cases, especially below the melting layer (Figure 14). Another common trend is that the area ratio of large hydrometeors within the melting layer top increases in twenty-six of thirty-three cases, does not change in six cases, and one case measurements are not available due to no large hydrometeors. The area ratio measurements are similarly consistent as hydrometeors transition from within the melting layer to below. The area ratio of small hydrometeors only increases through the melting layer bottom in two cases, is equal in twenty-seven cases, and decreases in one case. In the single case where the area ratio of small hydrometeors decreases, there is a region of much higher hydrometeor concentrations that is likely not associated with the melting layer (Figure 19). For large hydrometeors transitioning from within the melting layer to below, the area ratio increases in seven cases and stays the same in twenty.

Overall, the area ratio increase tends to be in the upper portion of the melting layer and is infrequently in the lower portion. In three of the cases where the ice-bulb temperature and air temperature both equal 0 °C at the melting layer top, the area ratio of small hydrometeors started to increase a small depth above the melting layer, compared to just one case with low relative humidity where the melting layer top is not at the 0 °C air temperature isotherm. The cause of area ratio starting to increase above the melting layer top is unknown. Speculatively, it’s possible that uncertainties in instrumentation cause the melting layer top to be at a higher altitude than identified. Additionally, the area ratio calculations from the SODA2 data processing for the HVPS3 may have led to inaccuracies. Similarly, the HVPS3 and other instruments may have experienced an uncorrected desync even if that is typically corrected for in the data processing. Hydrometeors could also have been round, even if frozen precipitation due to riming; although, this is unlikely because there are increases in area ratio from higher altitudes in each of the four cases.

Relative humidity appears to have little impact on the change in area ratio in the melting layer. The largest impact is on large hydrometeors. From above to within the melting layer, area ratio of large hydrometeors does not increase as frequently in lower relative humidity cases. In just two of twenty cases with relative humidity 95 percent and above, the area ratio of large hydrometeors does not change. Conversely, in four of thirteen cases with relative humidity below 95 percent, the area ratio does not change. Similarly, with relative humidity 95 percent and above, the area ratio of large hydrometeors increases from within the melting layer to below in seven of twenty cases compared to just one of thirteen cases where relative humidity is below 95 percent.

Changes in concentration are less consistent than area ratio changes; however, there are some common trends among the cases. In just one case, the concentration of large hydrometeors increases from above the melting layer to within. Conversely, in seventeen cases the concentration decreases and in fourteen cases the concentration stays the same. The decrease in concentration of large hydrometeors is likely due to hydrometeors becoming smaller during the melting process, shifting the concentration to smaller sizes. Additionally, it is expected that the concentration of small hydrometeors must increase due to conservation of mass. However, from above to within the melting layer, the concentration of small hydrometeors increases in just five cases, all of which are 94 percent and greater relative humidity, and three of which are saturated. Indeed, the concentration of small hydrometeors decreases in twenty cases while remaining roughly the same in six cases. It’s possible that the shift in concentration to hydrometeors smaller than 500 μm is from evaporation in the subsaturated air. However, two of six saturated cases have concentration of small hydrometeors decrease from above to within the melting layer. Heymsfield et al. (2015) found enhanced aggregation at the top of the melting layer, which explains a decrease in concentration of small hydrometeors. However, with enhanced aggregation there is an increase in concentration of large hydrometeors, increase in maximum diameter, and a decrease in both the intercept parameter and slope parameter from the exponential fit to the size distribution, which does not consistently occur in the cases where concentration of small hydrometeors decreases from above to within the melting layer. The inconsistency between these cases and results of Heymsfield et al. (2015) may be partially explained by their inclusion of a small hydrometeor imaging probe.

Like area ratio, hydrometeor concentration is mostly impacted during the early phases of melting as hydrometeors transition from above to within the melting layer. From within to below the melting layer, the concentration of large hydrometeors decreases in four cases and increases in just one case. There appears to be no relation between the change in hydrometeor concentration through the melting layer top and the decrease in concentration of large hydrometeors through the melting layer bottom. The change in concentration of small hydrometeors from within to below the melting layer is less consistent than large hydrometeor changes. The concentration decreases in five cases compared to increasing in three cases and equal in twenty-two cases. Relative humidity impacts hydrometeor concentration trends in the melting layer. Below 94 percent relative humidity, the concentration of all hydrometeors decreases or stays the same, whereas above 94 percent, the concentration changes vary. In these low relative humidity conditions, there is a loss of hydrometeor mass due to sublimation and evaporation in the melting layer resulting in lower concentrations.

The maximum diameter of hydrometeors is impacted by melting as hydrometeor size decreases from above to below the melting layer. During the transition from above to within the melting layer, the maximum diameter has no change in five cases, increases in eight, and decreases in twenty cases. Thus, in most cases the maximum diameter does not increase in the melting layer, suggesting there is no enhanced aggregation. The maximum diameter only increases in the subsaturated cases and is more frequent with lower relative humidity cases, suggesting that relative humidity may play a role in the aggregation of melting hydrometeors. From within the melting layer to below, the maximum diameter increases in just two cases, otherwise decreasing in seventeen cases and staying the same in twelve cases. Overall, from above to below the melting layer, the maximum diameter decreases in thirty cases.

The exponential fit of the HVPS3 size distribution has varying results due to the slope and intercept parameter having a large dependence on the concentration of hydrometeors. As the concentration of small hydrometeors increases, both parameters also increase. A larger maximum diameter, which often occurs above the melting layer or is a result of enhanced aggregation due to melting, causes a smaller slope parameter and slightly smaller intercept parameter. Conversely, at the melting layer bottom where maximum diameter is reduced in all but one case, the slope and intercept parameter increase. The most common trend is an increase in the slope parameter from above to within the melting layer in twenty seven cases, which contrasts results from Heymsfield et al. (2015) where the slope parameter decreased through the melting layer, but matches findings from Stewart et al. (1984) where the slope parameter only decreased until melting began. Similarly, the intercept parameter increases from above to within the melting layer in seventeen cases compared to staying the same in five cases and decreasing in eight cases. In all seventeen cases where the intercept parameter increases, the slope parameter also increases. However, the slope parameter also increases in six of the eight cases where the intercept parameter decreases.

The changes in the exponential fit parameters from within the melting layer to below are much more varied. The parameters experience an increase, decrease, and stay the same each in approximately a third of the cases. All three trends occur in the three cases where the slope parameter does not increase through the melting layer top. Thus, if the slope parameter does not increase in the upper portions of the melting layer, it will not necessarily increase in the lower portions of the melting layer. Similarly, if the intercept parameter does not increase through the melting layer top, it only increases through the melting layer bottom in just even of eighteen cases. Ultimately, the slope parameter is greater at the melting layer bottom compared to the top in twenty of the cases, while the intercept parameter is greater in fifteen cases. Overall, these results are most consistent with the exponential fit from (Stewart et al. 1984) where melting caused the slope parameter to increase; however, the decrease in small hydrometeor concentration likely caused the intercept parameter to increase less frequently. Although, in the two cases with significantly enhanced aggregation in the melting layer (IMPACTS_Spi-Des_94RH and MC3E_Ram-Asc_83RHa), both parameters decrease in the location of the increased maximum diameter, consistent with Heymsfield et al. (2015).

Given the trend variability of the exponential fit parameters in the melting layer, it is difficult to determine the impact from relative humidity. The intercept parameter increases less frequently for low relative humidity cases, likely a result of the size distribution shifting to smaller concentration values and thus smaller intercept. Additionally, the transition of the slope parameter from within to below the melting layer relates to relative humidity. For all thirteen cases below 95 percent relative humidity, the slope parameter decreases in six and stays the same in four (with no measurements for three cases). At 95 percent relative humidity and above, the slope parameter decreases from within to below the melting layer in just five of twenty cases compared to increasing in ten cases and staying the same in five.

Grouped cases highlights how relative humidity impacts transitions above, within, and below the melting layer. Overall, the saturated cases are not much different than the high relative humidity cases and more differences arise in the low relative humidity cases. The changes in area ratio due to melting are largely unimpacted by relative humidity – hydrometeors eventually become round, whether conditions are relatively dry or moist. Relative humidity impacts the concentration of hydrometeors as dry conditions lead to consistently decreased hydrometeor concentrations and more frequently reduces both exponential fit parameters. Finally, enhanced aggregation is most common in lower relative humidity conditions.

CHAPTER 6

CONCLUSIONS

The area ratio of hydrometeors describes their roundness and is an indicator for melting as ice hydrometeors with low area ratios increase during melting. In-situ probe images of hydrometeors within the melting layer have area ratio increases that are first apparent in smaller hydrometeors as the temperature increases. Typically, area ratio increases from the 0.3 to 0.5 range to approximately 0.8, which matches the raindrop value from Heymsfield et al. (2015); however, sometimes the area ratio of frozen hydrometeors varies and melted hydrometeors have area ratio below 0.8. Therefore, an increase in area ratio over a depth best indicates that melting is occurring. However, in eight of the thirty-three identified melting layer cases, manual review of images indicates a lower bottom altitude than the area ratio indicates since infrequent large sized hydrometeors do not appear round in images.

In subsaturated conditions where there is a difference between the 0 °C air temperature and ice-bulb isotherm, the area ratio does not begin to increase until below the 0 °C ice-bulb isotherm, which confirms Heymsfield et al. (2021) assessment that an ice-bulb temperature of 0 °C is an accurate depiction of the melting layer top. Numerical models could benefit from implementing a melting layer top defined by the 0 °C ice-bulb isotherm. Additionally, models should not necessarily include a common report that the melting layer is associated with a 0 °C isothermal or quasi-isothermal layer (e.g., Wexler et al. 1954; Atlas et al. 1969; Carbone 1982; Stewart et al. 1984; Szeto and Stewart 1997; Kain et al. 2000) as only two of the thirty-three cases had a 0 °C quasi-isothermal layer, and one of them is solely above the melting layer (Figure 23). The cloud type and environment may play a significant role in the development of a quasi-isothermal layer due to melting. Diabatic cooling due to melting is parameterized in numerical model microphysics schemes, and ensuring that the cooling rate is representative of observations is important for better forecasts. Another avenue for future studies is to assess how melting impacts the lapse rate. While the onset of melting may not always create a 0 °C quasi-isothermal layer, it may instead lower the lapse rate, which would deepen the melting layer and better match results of previous studies.

The concentration of large hydrometeors decreases from above to below the melting layer; however, the concentration of small hydrometeors infrequently increases, which suggests hydrometeors evaporate and the concentration is shifted to hydrometeors smaller than 500 μm. Another common result is a lack of strongly enhanced aggregation in the melting layer, which had been hypothesized as a potential cause of the radar bright band signal (e.g., Austin and Bemis 1950; Klaassen 1988; Willis and Heymsfield 1989; Heymsfield et al. 2015). Additional analysis could compare bright band signal to the reflectivity changes due to the observed change in hydrometeor concentration. The exponential spectrum fit is largely variable with the most common trend being the slope parameter increase in the melting layer, which suggests no significant aggregation is occurring. Although, future studies may also consider fitting the spectrum to a gamma distribution and combining the large and small probe observations.

An analysis limitation is the low resolution images used to derive area ratio for small sized hydrometeors. While the 2D-S has 10 μm diodes, the melting layer 2D-S observations frequently measured zero hydrometeors and derived measurements are not used. The ability of the HVPS3 to measure hydrometeors that the 2D-S did not in the 300 to 2000 μm range is due to the larger HVPS3 sample volume. A larger sample volume probe with higher resolution than the HVPS3, such as the SPEC Hawkeye Combination Cloud Hydrometeor Probe which includes a new 50 μm channel of the 2D-S may improve the profile of small hydrometeors and their transition within the melting layer for future studies.

APPENDIX A

Ice-bulb and Wet-bulb Temperature Calculations

The ice-bulb and wet-bulb temperatures are calculated with the newly developed Airborne Data Processing and Analysis (ADPAA) module, bulbtemp.py. The bulbtemp module procedures a file with ice-bulb and wet-bulb temperatures using inputs of atmospheric pressure, temperature, and dew point temperature. The bulbtemp module utilizes the fsolve numerical solver, which is part of the SciPy Python module.

The fsolve solver provides roots of a non-linear equation or system of equations. For the ice-bulb and wet-bulb temperatures calculations, fsolve is used to determine roots of two non-linear equations derived from the Clausius-Clapeyron equation and the psychrometric formula. The psychrometric formula, sometimes referred to as the hygrometric formula, gives the vapor pressure from barometer and psychrometer readings (AMS Glossary of Meteorology). The Clausius-Clapeyron equation relates air temperature (T) and saturation vapor pressure (e_s) as,

$$e_s(T) = e_0 \exp\left[\frac{l_v}{R_v}\left(\frac{1}{T_0} - \frac{1}{T}\right)\right] \tag{A1}$$

Additionally, the Clausius-Clapeyron equation relates dew point temperature (T_d) and vapor pressure (e) as,

$$e(T_d) = e_0 \exp\left[\frac{l_v}{R_v}\left(\frac{1}{T_0} - \frac{1}{T_d}\right)\right] \tag{A2}$$

where e_0 = 6.11 hPa is the vapor pressure at the triple point of water, $l_v = 2.501 \times 10^6$ J/kg is the latent heat of vaporization, R_v = 461.5 J/kg/K is the gas constant for moist air, and T_0 = 273.16 K is the air temperature at the triple point of water.

The saturation vapor pressure at the ice-bulb (e_{IB}) and wet-bulb (e_{WB}) temperatures follows the form of (A1) and (A2) as a function of ice-bulb temperature (T_{IB}) and wet-bulb temperature (T_{WB}), respectively and are given by

$$e_{IB}(T_{IB}) = e_0 \exp\left[\frac{l_v}{R_v}\left(\frac{1}{T_0} - \frac{1}{T_{IB}}\right)\right] \tag{A3}$$

$$e_{WB}(T_{WB}) = e_0 \exp\left[\frac{l_v}{R_v}\left(\frac{1}{T_0} - \frac{1}{T_{WB}}\right)\right] \tag{A4}$$

The ice-bulb and wet-bulb saturation vapor pressure equations (A3) and (A4) are rearranged to equal zero by subtracting the vapor pressure on both sides to provide

$$e_0 \exp\left[\frac{l_v}{R_v}\left(\frac{1}{T_0} - \frac{1}{T_{IB}}\right)\right] - e_{IB}(T_{IB}) = 0 \tag{A5}$$

$$e_0 \exp\left[\frac{l_v}{R_v}\left(\frac{1}{T_0} - \frac{1}{T_{WB}}\right)\right] - e_{WB}(T_{WB}) = 0 \tag{A6}$$

(A5) and (A6) is the equation form used in fsolve.

The psychrometric formula relates the vapor pressure to atmospheric pressure, air temperature, saturation vapor pressure at the ice-bulb or wet-bulb temperature and are given by

$$e = e_{IB}(T_{IB}) - 5.82 \times 10^{-4}\,(1 + 0.00115\,\mathrm{T_w})\,\mathrm{p}\,(\mathrm{T} - \mathrm{T_w}) \tag{A7}$$

$$e = e_{WB}(T_{WB}) - 6.60 \times 10^{-4}\,(1 + 0.00115\,\mathrm{T_w})\,\mathrm{p}\,(\mathrm{T} - \mathrm{T_w}) \tag{A8}$$

The psychrometric formulas (A7) and (A8) are similarly rearranged to equal zero by subtracting vapor pressure from both sides to get the form used in the numerical solver,

$$e_{IB}(T_{IB}) - 5.82 \times 10^{-4} (1 + 0.00115\ \mathrm{T_w})\ \mathrm{p}\ (\mathrm{T} - \mathrm{T_w}) = 0 \tag{A9}$$

$$e_{WB}(T_{WB}) - 6.60 \times 10^{-4} (1 + 0.00115\ \mathrm{T_w})\ \mathrm{p}\ (\mathrm{T} - \mathrm{T_w}) = 0 \tag{A10}$$

The numerical solver returns the ice-bulb temperature using (A5) and (A9) and the wet-bulb temperature using (A6) and (A10).

To verify the accuracy of the bulbtemp module, results of the wet-bulb calculation are compared to the wet-bulb calculation from the MetPy Python module (Table A1). The MetPy module provides the wet-bulb temperature by lifting a parcel to the lifting condensation level and returning it to the original pressure level in a pseudoadiabatic process, as would be done in a Skew-T Log-P diagram. The difference between the bulbtemp and MetPy modules is small for high relative humidity. The ice-bulb and wet-bulb temperatures equal air temperature when the relative humidity is 100 percent, hence only up to 99 percent relative humidity is compared. Choosing the pressure levels of 500 hPa and 1000 hPa allows for comparison of the results to figure 1 in Heymsfield et al. (2021). For temperatures between 0 °C and 10 °C and relative humidity ranging from 25 percent to 100 percent, bulbtemp deviates slightly from the ice-bulb temperature calculation from Heymsfield et al. (2021). For both 500 hPa and 1000 hPa, bulbtemp has a maximum deviation of about 0.3 °C higher. The differences are minimized for lower temperatures approaching 0 °C and higher relative humidity values approaching 100 percent. Notably, the bulbtemp ice-bulb temperature is closer to the ice-bulb temperature calculation from Heymsfield et al. (2021) than the MetPy wet-bulb temperature results.

The developed bulbtemp module efficiently computes wet-bulb and ice-bulb temperatures and works for large datasets such as the in-situ data described in Chapter 2. With the implementation of bulbtemp in ADPAA and its relatively close agreement with other calculations, it is the module used to calculate the ice-bulb temperature for the in-situ observations.

Table A1: Table showing ice-bulb and wet-bulb temperature calculations for relative humidity (RH) ranging from 70 to 99 percent for the two pressure levels of 500 and 1,000 hPA and temperatures ranging from 0 to 10 °C. The wet-bulb difference (Diff.) is the MetPy calculated wet-bulb (Wet-bulb) substracted from the MetPy's wet_bulb (MetPy Wet-bulb) given in the last column.

RH	Pressure	Temp	Ice-bulb	Wet-bulb	MetPy Wet-bulb	Diff.
%	*hPA*	*℃*	*℃*	*℃*	*℃*	*℃*
70	**500**	0.0	-1.5	-1.4	-1.7	0.3
		2.0	0.3	0.4	0.1	0.3
		4.0	2.1	2.3	1.9	0.4
		6.0	4.0	4.1	3.7	0.4
		8.0	5.8	5.9	5.6	0.3
		10.0	7.6	7.8	7.4	0.4
	1000	0.0	-2.3	-2.2	-2.5	0.3
		2.0	-0.5	-0.3	-0.7	0.4
		4.0	1.3	1.5	1.1	0.4
		6.0	3.1	3.3	2.9	0.4
		8.0	4.9	5.1	4.7	0.4
		10.0	6.8	6.9	6.5	0.4
80	**500**	0.0	-1.0	-0.9	-1.1	0.2
		2.0	0.9	1.0	0.7	0.3
		4.0	2.8	2.9	2.6	0.3
		6.0	4.7	4.7	4.5	0.2
		8.0	6.5	6.6	6.4	0.2
		10.0	8.4	8.5	8.3	0.2
	1000	0.0	-1.5	-1.4	-1.7	0.3
		2.0	0.4	0.5	0.2	0.3
		4.0	2.2	2.3	2.1	0.2
		6.0	4.1	4.2	4.0	0.2
		8.0	6.0	6.1	5.9	0.2
		10.0	7.9	8.0	7.8	0.2
90	**500**	0.0	-0.5	-0.5	-0.6	0.1
		2.0	1.4	1.5	1.4	0.1
		4.0	3.4	3.4	3.3	0.1
		6.0	5.3	5.4	5.3	0.1
		8.0	7.3	7.3	7.2	0.1
		10.0	9.2	9.3	9.2	0.1
	1000	0.0	-0.7	-0.7	-0.8	0.1
		2.0	1.2	1.2	1.1	0.1
		4.0	3.1	3.2	3.1	0.1
		6.0	5.1	5.1	5.0	0.1
		8.0	7.0	7.1	7.0	0.1
		10.0	9.0	9.0	8.9	0.1

99	**500**	0.0	-0.1	0.0	-0.1	0.1
		2.0	1.9	1.9	1.9	0.0
		4.0	3.9	3.9	3.9	0.0
		6.0	5.9	5.9	5.9	0.0
		8.0	7.9	7.9	7.9	0.0
		10.0	9.9	9.9	9.9	0.0
	1000	0.0	-0.1	-0.1	-0.1	0.0
		2.0	1.9	1.9	1.9	0.0
		4.0	3.9	3.9	3.9	0.0
		6.0	5.9	5.9	5.9	0.0
		8.0	7.9	7.9	7.9	0.0
		10.0	9.9	9.9	9.9	0.0

APPENDIX B

Additional Field Campaigns

List and table of additional field campaigns where data would need to be processed with ADPAA.

Table B1: Table showing the dates and times in seconds from midnight (sfm) of potential melting layer profiles from the additional field campaigns.

Project	**Date**	**Start**	**End**
	YYYMMDD	*sfm*	*sfm*
	20100916	38400	38520
	20101020	35040	35100
	20010924	96840	97020
	20010909	71040	71220
	20010909	71580	71400
	20020726	78540	78720
	20020726	81060	81240
	20020726	81660	81540
	20020726	83760	83880
	20060903	48900	48720
	20060903	48240	48540
	20060912	54660	54900
	20070717	72420	72600
	20070808	69180	69060

REFERENCES

Atlas, D., R. Tatehira, R. C. Srivastava, W. Marker, and R. E. Carbone, 1969: Precipitation-induced mesoscale wind perturbations in the melting layer. *Quarterly Journal of the Royal Meteorological Society*, **95**, 544–560, https://doi.org/10.1002/qj.49709540508.

Austin, P. M., and A. C. Bemis, 1950: A QUANTITATIVE STUDY OF THE "BRIGHT BAND" IN RADAR PRECIPITATION ECHOES. *Journal of the Atmospheric Sciences*, **7**, 145–151, https://doi.org/10.1175/1520-0469(1950)007<0145:AQSOTB>2.0.CO;2.

Baeck, M. L., and J. A. Smith, 1998: Rainfall Estimation by the WSR-88D for Heavy Rainfall Events. *Weather and Forecasting*, **13**, 416–436, https://doi.org/10.1175/1520-0434(1998)013<0416:REBTWF>2.0.CO;2.

Battan, L., 1973: Radar observation of the atmosphere. *University of Chicago Press*, 324, https://doi.org/10.1002/qj.49709942229.

Carbone, R. E., 1982: A Severe Frontal Rainband. Part I. Stormwide Hydrodynamic Structure. *Journal of the Atmospheric Sciences*, **39**, 258–279, https://doi.org/10.1175/1520-0469(1982)039<0258:ASFRPI>2.0.CO;2.

Carlin, J. T., and A. V. Ryzhkov, 2019: Estimation of Melting-Layer Cooling Rate from Dual-Polarization Radar: Spectral Bin Model Simulations. *Journal of Applied Meteorology and Climatology*, **58**, 1485–1508, https://doi.org/10.1175/JAMC-D-18-0343.1.

Chen, H., and V. Chandrasekar, 2014: Estimation of rainfall drop size distribution from dual-polarization measurements at S-band, X-band, and Ku-band radar frequencies. *2014 IEEE Geoscience and Remote Sensing Symposium*, 2014 IEEE Geoscience and Remote Sensing Symposium, 4978–4981.

Delene, D. J., 2011: Airborne data processing and analysis software package. *Earth Sci Inform*, **4**, 29–44, https://doi.org/10.1007/s12145-010-0061-4.

Ding, B., K. Yang, J. Qin, L. Wang, Y. Chen, and X. He, 2014: The dependence of precipitation types on surface elevation and meteorological conditions and its parameterization. *Journal of Hydrology*, **513**, 154–163, https://doi.org/10.1016/j.jhydrol.2014.03.038.

Fabry, F., and I. Zawadzki, 1995: Long-Term Radar Observations of the Melting Layer of Precipitation and Their Interpretation. *Journal of the Atmospheric Sciences*, **52**, 838–851, https://doi.org/10.1175/1520-0469(1995)052<0838:LTROOT>2.0.CO;2.

Findeisen, W., 1940: The formation of the 0°C isothermal layer and fractocumulus under nimbostratus. *Meteor. Z.*, **57**, 49–54.

Freud, E., D. Rosenfeld, and J. R. Kulkarni, 2011: Resolving both entrainment-mixing and number of activated CCN in deep convective clouds. *Atmospheric Chemistry and Physics*, **11**, 12887–12900, https://doi.org/10.5194/acp-11-12887-2011.

Fujiyoshi, Y., 1986: Melting Snowflakes. *Journal of the Atmospheric Sciences*, **43**, 307–311, https://doi.org/10.1175/1520-0469(1986)043<0307:MS>2.0.CO;2.

Gorgucci, E., L. Baldini, and V. Chandrasekar, 2006: What Is the Shape of a Raindrop? An Answer from Radar Measurements. *Journal of the Atmospheric Sciences*, **63**, 3033–3044, https://doi.org/10.1175/JAS3781.1.

Guo, X., C. Lu, T. Zhao, G. J. Zhang, and Y. Liu, 2015: An Observational Study of Entrainment Rate in Deep Convection. *Atmosphere*, **6**, 1362–1376, https://doi.org/10.3390/atmos6091362.

Harrison, D. L., S. J. Driscoll, and M. Kitchen, 2000: Improving precipitation estimates from weather radar using quality control and correction techniques. *Meteorological Applications*, **7**, 135–144, https://doi.org/10.1017/S1350482700001468.

Heymsfield, A. J., and J. L. Parrish, 1978: A Computational Technique for Increasing the Effective Sampling Volume of the PMS Two-Dimensional Particle Size Spectrometer. *Journal of Applied Meteorology and Climatology*, **17**, 1566–1572, https://doi.org/10.1175/1520-0450(1978)017<1566:ACTFIT>2.0.CO;2.

——, A. Bansemer, P. R. Field, S. L. Durden, J. L. Stith, J. E. Dye, W. Hall, and C. A. Grainger, 2002: Observations and Parameterizations of Particle Size Distributions in Deep Tropical Cirrus and Stratiform Precipitating Clouds: Results from In Situ Observations in TRMM Field Campaigns. *Journal of the Atmospheric Sciences*, **59**, 3457–3491, https://doi.org/10.1175/1520-0469(2002)059<3457:OAPOPS>2.0.CO;2.

——, ——, M. R. Poellot, and N. Wood, 2015: Observations of Ice Microphysics through the Melting Layer. *Journal of the Atmospheric Sciences*, **72**, 2902–2928, https://doi.org/10.1175/JAS-D-14-0363.1.

——, ——, A. Theis, and C. Schmitt, 2021: Survival of Snow in the Melting Layer: Relative Humidity Influence. *Journal of the Atmospheric Sciences*, https://doi.org/10.1175/JAS-D-20-0353.1.

Igel, A. L., and S. C. van den Heever, 2014: The role of latent heating in warm frontogenesis: The Role of Latent Heating in Warm Frontogenesis. *Q.J.R. Meteorol. Soc.*, **140**, 139–150, https://doi.org/10.1002/qj.2118.

Iversen, E. C., G. Thompson, and B. E. Nygaard, 2021: Improvements to melting snow behavior in a bulk microphysics scheme. *Atmospheric Research*, **253**, 105471, https://doi.org/10.1016/j.atmosres.2021.105471.

Joos, H., and H. Wernli, 2012: Influence of microphysical processes on the potential vorticity development in a warm conveyor belt: a case-study with the limited-area model COSMO. *Quarterly Journal of the Royal Meteorological Society*, **138**, 407–418, https://doi.org/10.1002/qj.934.

Kain, J. S., S. M. Goss, and M. E. Baldwin, 2000: The Melting Effect as a Factor in Precipitation-Type Forecasting. *Weather and Forecasting*, **15**, 700–714, https://doi.org/10.1175/1520-0434(2000)015<0700:TMEAAF>2.0.CO;2.

Khain, A., M. Ovtchinnikov, M. Pinsky, A. Pokrovsky, and H. Krugliak, 2000: Notes on the state-of-the-art numerical modeling of cloud microphysics. *Atmospheric Research*, **55**, 159–224, https://doi.org/10.1016/S0169-8095(00)00064-8.

Klaassen, W., 1988: Radar Observations and Simulation of the Melting Layer of Precipitation. *J. Atmos. Sci.*, **45**, 3741–3753, https://doi.org/10.1175/1520-0469(1988)045<3741:ROASOT>2.0.CO;2.

Knight, C. A., 1979: Observations of the Morphology of Melting Snow. *Journal of the Atmospheric Sciences*, **36**, 1123–1130, https://doi.org/10.1175/1520-0469(1979)036<1123:OOTMOM>2.0.CO;2.

Knollenberg, R. G., 1981: TECHNIQUES FOR PROBING CLOUD MICROSTRUCTURE. *Clouds their Formation, Optical Properties, and Effects*, P.V. Hobbs and A. Deepak, Eds., Academic Press, 15–91.

Kumjian, M. R., S. Mishra, S. E. Giangrande, T. Toto, A. V. Ryzhkov, and A. Bansemer, 2016: Polarimetric radar and aircraft observations of saggy bright bands during MC3E. *Journal of Geophysical Research: Atmospheres*, **121**, 3584–3607, https://doi.org/10.1002/2015JD024446.

Lawson, R. P., R. E. Stewart, and L. J. Angus, 1998: Observations and Numerical Simulations of the Origin and Development of Very Large Snowflakes. *Journal of the Atmospheric Sciences*, **55**, 3209–3229, https://doi.org/10.1175/1520-0469(1998)055<3209:OANSOT>2.0.CO;2.

——, D. O'Connor, P. Zmarzly, K. Weaver, B. Baker, Q. Mo, and H. Jonsson, 2006: The 2D-S (Stereo) Probe: Design and Preliminary Tests of a New Airborne, High-Speed, High-Resolution Particle Imaging Probe. *Journal of Atmospheric and Oceanic Technology*, **23**, 1462–1477, https://doi.org/10.1175/JTECH1927.1.

Leinonen, J., and A. von Lerber, 2018: Snowflake Melting Simulation Using Smoothed Particle Hydrodynamics. *Journal of Geophysical Research: Atmospheres*, **123**, 1811–1825, https://doi.org/10.1002/2017JD027909.

Lin, C. A., and R. E. Stewart, 1986: Mesoscale circulations initiated by melting snow. *J. Geophys. Res.*, **91**, 13299, https://doi.org/10.1029/JD091iD12p13299.

——, and ——, 1991: Diabatically Forced Mesoscale Circulations in the Atmosphere. *Advances in Geophysics*, Vol. 33 of, Elsevier, 267–305.

Marshall, J. S., and W. M. K. Palmer, 1948: THE DISTRIBUTION OF RAINDROPS WITH SIZE. *Journal of the Atmospheric Sciences*, **5**, 165–166, https://doi.org/10.1175/1520-0469(1948)005<0165:TDORWS>2.0.CO;2.

Matsuo, T., and Y. Sasyo, 1981: Empirical formula for the melting rate of snowflakes. https://doi.org/10.2151/JMSJ1965.59.1_1.

McFarquhar, G. M., M. S. Timlin, R. M. Rauber, B. F. Jewett, J. A. Grim, and D. P. Jorgensen, 2007: Vertical Variability of Cloud Hydrometeors in the Stratiform Region of Mesoscale Convective Systems and Bow Echoes. *Monthly Weather Review*, **135**, 3405–3428, https://doi.org/10.1175/MWR3444.1.

Mitra, S. K., O. Vohl, M. Ahr, and H. R. Pruppacher, 1990: A Wind Tunnel and Theoretical Study of the Melting Behavior of Atmospheric Ice Particles. IV: Experiment and Theory for Snow Flakes. *Journal of the Atmospheric Sciences*, **47**, 584–591, https://doi.org/10.1175/1520-0469(1990)047<0584:AWTATS>2.0.CO;2.

Morrison, H., J. A. Milbrandt, G. H. Bryan, K. Ikeda, S. A. Tessendorf, and G. Thompson, 2015: Parameterization of Cloud Microphysics Based on the Prediction of Bulk Ice Particle Properties. Part II: Case Study Comparisons with Observations and Other Schemes. *Journal of the Atmospheric Sciences*, **72**, 312–339, https://doi.org/10.1175/JAS-D-14-0066.1.

Stewart, R. E., J. D. Marwitz, J. C. Pace, and R. E. Carbone, 1984: Characteristics through the Melting Layer of Stratiform Clouds. *Journal of the Atmospheric Sciences*, **41**, 3227–3237, https://doi.org/10.1175/1520-0469(1984)041<3227:CTTMLO>2.0.CO;2.

Szeto, K. K., and R. E. Stewart, 1997: Effects of Melting on Frontogenesis. *Journal of the Atmospheric Sciences*, **54**, 689–702, https://doi.org/10.1175/1520-0469(1997)054<0689:EOMOF>2.0.CO;2.

Szyrmer, W., and I. Zawadzki, 1999: Modeling of the Melting Layer. Part I: Dynamics and Microphysics. *Journal of the Atmospheric Sciences*, **56**, 3573–3592, https://doi.org/10.1175/1520-0469(1999)056<3573:MOTMLP>2.0.CO;2.

Tapiador, F. J., J.-L. Sánchez, and E. García-Ortega, 2019: Empirical values and assumptions in the microphysics of numerical models. *Atmospheric Research*, **215**, 214–238, https://doi.org/10.1016/j.atmosres.2018.09.010.

Thompson, G., P. R. Field, R. M. Rasmussen, and W. D. Hall, 2008: Explicit Forecasts of Winter Precipitation Using an Improved Bulk Microphysics Scheme. Part II: Implementation of a New Snow Parameterization. *Monthly*

Weather Review, **136**, 5095–5115, https://doi.org/10.1175/2008MWR2387.1.

Wagner, S. W., and D. J. Delene, 2022: *Technique for comparison of backscatter coefficients derived from in-situ cloud probe measurements with concurrent airborne Lidar*. Clouds/In Situ Measurement/Validation and Intercomparisons,.

Wexler, R., R. J. Reed, and J. Honig, 1954: Atmospheric Cooling by Melting Snow *. *Bulletin of the American Meteorological Society*, **35**, 48–51, https://doi.org/10.1175/1520-0477-35.2.48.

Willis, P. T., and A. J. Heymsfield, 1989: Structure of the Melting Layer in Mesoscale Convective System Stratiform Precipitation. *Journal of the Atmospheric Sciences*, **46**, 2008–2025, https://doi.org/10.1175/1520-0469(1989)046<2008:SOTMLI>2.0.CO;2.

Psychrometric formula - Glossary of Meteorology. https://glossary.ametsoc.org/wiki/Psychrometric_formula (Accessed May 2, 2022).